How endosomal PIKfyve inhibition prevents viral membrane fusion and entry

Nicholas Chow[1,$], Gustavo Scanavachi[1,2,3,$], Anand Saminathan[1,2,$] and Tom Kirchhausen[1,2,3,*]

[1]Program in Cellular and Molecular Medicine, Boston Children's Hospital, 200 Longwood Ave, Boston, MA 02115, USA
[2]Department of Cell Biology, Harvard Medical School, 200 Longwood Ave, Boston, MA 02115, USA
[3]Department of Pediatrics, Harvard Medical School, 200 Longwood Ave, Boston, MA 02115, USA

[$] Equal contribution

[*] Corresponding author:
Tom Kirchhausen. Ph.D.
Harvard Medical School
200 Longwood Ave
Boston, MA 02115
kirchhausen@crystal.harvard.edu
phone: +1 617 713 8888 / fax: +1 617 713 8898

Running title: *Swollen Endosomes Block Productive Viral Fusion and Entry*

Key words: *Viral Entry, PIKfyve Inhibition, Endosomal Fusion, Membrane Tension, Lattice Light-Sheet Microscopy*

ABSTRACT

Enveloped viruses enter cells by membrane fusion. The viral membrane fuses with a host membrane, either at the cell surface or within endocytic compartments. For endocytic entry, fusion is typically triggered by low pH and often requires proteolytic priming by compartment-specific host proteases, which together define the site and mechanism of fusion and shape viral tropism.

Inhibition of the lipid kinase PIKfyve, which generates PI(5)P and PI(3,5)P_2 in late endosomes and lysosomes, swells those compartments and blocks infection by a subset of enveloped viruses, including Ebola virus, Marburg virus, coronaviruses (SARS-CoV-2), and VSV chimeras bearing Ebola, SARS-CoV-2, or Lassa glycoproteins, while showing minor effects on H1N1 influenza and no effect on VSV or VSV–rabies chimeras. In the work reported here, we have determined the basis for this selectivity.

We show that swelling of late endosomes/lysosomes, independent of changes in lipid composition or altered virion trafficking, is sufficient to block virus–endosome fusion and genome release, even when endosomal acidity is preserved. Acute PIKfyve inhibition with apilimod or brief hypotonic treatment produced endosomal swelling and impaired infection by interrupting a late endosomal entry step. Imaging by live-cell 3D lattice light-sheet fluorescence microscopy tracked fluorescent virions accumulating and arresting in late endosomes prior to fusion, and single-cell, single-round assays confirmed loss of infectivity.

These data support a simple biophysical mechanism: endo-lysosomal swelling, likely increasing endosomal membrane tension, creates an energy barrier to fusion and genome release. Inducing such swelling may offer a general strategy to inhibit viruses that depend on late endosomal entry.

INTRODUCTION

Enveloped viruses initiate infection by fusing their membrane with a host-cell membrane, delivering their genetic material into the cytosol (see review [1]). This fusion can occur at the plasma membrane or within endocytic compartments. For many viruses, including filoviruses and coronaviruses that rely on endocytosis, fusion is typically triggered by low endosomal pH and often requires proteolytic priming of viral glycoproteins by endosomal resident host proteases; for some, an additional host factor in the endolysosomal compartment is required (see reviews [2–5]). These spatial and pH dependencies define the site and mechanism of fusion during the early steps of infection, and, ultimately, determine viral tropism and infectivity.

PIKfyve, a lipid kinase on late endosomal and lysosomal membranes, generates phosphatidylinositol 3,5-bisphosphate [PI(3,5)P_2]. Its depletion or pharmacological inhibition produces enlarged late endosomes and lysosomes [6–9] and blocks early steps of infection by a subset of enveloped viruses. PIKfyve inhibition blocks infection by a various enveloped viruses at early stages of entry. For example, apilimod inhibits GP-mediated entry of filoviruses and SARS-CoV-2, both for authentic viruses and for VSV- or lentivirus-based pseudotypes, without affecting virion uptake or bulk endosomal acidification [10,11]. Vacuolin-1, which also targets PIKfyve, similarly suppresses single-cycle infection by VSV chimeras bearing Ebola or SARS-CoV-2 glycoproteins by preventing fusion and genome delivery from endolysosomal compartments [11]. Other PIKfyve-directed compounds, including YM201636, the selective probe SGC-PIKFYVE-1, and a dual PIKfyve/PIP5K1C inhibitor, inhibit early infection by parental African swine fever virus, enteroviruses, and β-coronaviruses, as well as by SARS-CoV-2 spike–pseudotyped virions [12–15]. Together, these observations support the view that PIKfyve-activity at late endosomes and lysosomes is a common requirement for successful viral entry. In contrast, PIKfyve inhibition has only modest effects on H1N1 influenza virus infection[16] and little or no effect on viruses whose entry occurs in early endosomes, such as VSV and VSV particles bearing rabies virus G (VSV–RABV) [11].

A recent study identified LYVAC (PDZD8) as the ER-anchored lipid transfer protein that mediates ER-to-lysosome lipid transfer at ER–endolysosome contact sites, enabling osmotic membrane expansion [17]. In the absence of LYVAC, apilimod fails to induce lysosomal swelling, supporting a model in which vacuolation depends on lipid transfer and the consequent increase in membrane tension, rather than on loss of PI3P or PI(3,5)P_2. We therefore tested the hypothesis that the antiviral effect of PIKfyve inhibition by apilimod arises primarily from a mechanical constraint on

fusion, rather than from a block in endosomal trafficking or a change in endosomal phosphoinositide composition. We combined quantitative infectivity assays with high-precision, live-cell three-dimensional fluorescence microscopy to track single virions, allowing direct comparison of the effects of apilimod on VSV, VSV–ZEBOV, and VSV–SARS-CoV-2 infection.

Because these viruses share an identical VSV backbone, differences in apilimod sensitivity must arise from how their entry steps respond to perturbation of PIKfyve activity rather than from downstream replication events. Entry of VSV is mediated by its G protein and requires no further proteolysis for activation. Following clathrin-mediated endocytosis, acidification in early and early–late endosomes triggers a conformational change in G that drives membrane fusion. In contrast, VSV–ZEBOV requires two sequential processing steps of its GP: cleavage during biosynthesis, followed by cathepsin-mediated trimming in late endosomes or lysosomes to expose the NPC1-binding site. VSV–SARS-CoV-2 likewise depends on sequential proteolysis of its spike protein, furin cleavage at S1/S2 during maturation, followed by TMPRSS2- or cathepsin-mediated cleavage at S2′ and on endosomal acidification.

We show here that endosomal swelling, induced either by apilimod or by hypoosmotic challenge, correlates with inhibition of viral fusion, but only for VSV–ZEBOV or VSV–SARS-CoV-2 virions that reach and attempt fusion within swollen compartments. VSV, which enters from early endosomes that do not swell, escapes this inhibition, as does a subpopulation of VSV–SARS-CoV-2 virions that fuse in early endosomes. We suggest that under these swelling conditions, endolysosomes accumulate solute and water and increase their volume without a fully compensatory increase in membrane area. The resulting rise in membrane tension will oppose the local membrane remodeling required for fusion [1]. Increased membrane tension in swollen compartments thus imposes a physical barrier to fusion and thereby accounts for the selective sensitivity of certain viruses to PIKfyve inhibition.

RESULTS

Apilimod inhibits infection by VSV-eGFP-SARS-CoV-2 and VSV-MeGFP-ZEBOV but not by VSV-eGFP

We first confirmed that infection by VSV-SARS-CoV-2 or VSV-ZEBOV requires PIKfyve activity, whereas infection by VSV-G does not. We inoculated Vero cells not expressing TMPRSS2 with three recombinant VSVs: (i) VSV-eGFP-G, which expresses soluble eGFP and the parental VSV G protein; (ii) VSV-eGFP–SARS-CoV-2, which expresses soluble eGFP and in which the SARS-CoV-2 spike replaces G; and (iii) VSV-MeGFP–ZEBOV, which expresses eGFP fused to the viral matrix protein (M) and carries the Zaire ebolavirus GP instead of G. All three viruses deliver their genomes into the cytosol by low pH–triggered fusion from endosomal compartments following endocytosis [11].

We measured infectivity in Vero cells using a single-cell imaging assay that reports expression of virally encoded cytosolic eGFP or MeGFP [11], following the incubation protocol shown in Fig. 1A. To assess the role of endosomal PIKfyve on infection, we treated the Vero cells with apilimod, a selective inhibitor of PIKfyve lipid kinase activity. As shown in Figs. 1B-D, apilimod fully inhibited infection by VSV-eGFP–SARS-CoV-2 and VSV-MeGFP–ZEBOV but had no effect on VSV-eGFP-G.

Compartment-specific endosomal swelling

Apilimod treatment of SVG-A cells co-expressing fluorescent chimeras of mScarlet-EEA1 (a marker of early endosomes) and NPC-1-Halo (a marker of late endosomes and lysosomes) causes swelling of the latter compartment(s), but not of the former [11]. We confirmed here that we can detect this compartment-specific swelling in SVG-A cells by lattice light-sheet microscopy (LLSM) (Fig. S1). After apilimod treatment, endosomes labeled with mScarlet alone remained as small, diffraction limited puncta, while those labeled with NPC-1-Halo, as well as those containing both labels, became substantially enlarged.

We examined dose dependence of enlargement as follows. We loaded cells with Alexa Fluor 568-labeled dextran (Dextran-AF568), which accumulates in late endosomes and lysosomes, and measured the radii of individual endolysosomes across a range of apilimod concentrations (Fig.2). In untreated cells, late endosomes and lysosomes had a narrow distribution of radii centered at ~0.5μm (range 0.3-1.0μm: Fig. 2 B,C). Apilimod induced a concentration-dependent increase in radius, yielding a bimodal distribution with peaks centered at ~0.75μm

159 and at ~1.25μm. Applying a 90th percentile cutoff (0.725μm) to score a position as "swollen"
160 yielded the dose-dependent frequency of enlargement shown in Fig. 2 C,D).
161
162 **Apilimod-induced late-endosomal swelling inhibits entry of VSV-MeGFP-ZEBOV and**
163 **VSV-eGFP-SARS-CoV-2 but not of VSV itself**
164 We verified that incoming VSV-MeGFP-ZEBOV particles reach NPC-1 compartments under our
165 experimental conditions by using LLSM with genome-edited SVG-A cells expressing NPC1-Halo
166 [11] labelled with Janelia Fluor 646 HaloTag. Cells were exposed to virions for 10 min, washed, and
167 imaged 40 min or 4 hrs. later at 37 °C, according to the protocol in Fig. 3A. At a multiplicity of
168 infection (MOI) of ~0.5, each cell imaged at 40 min post inoculation contained 25–30 fluorescent
169 virions in NPC1-positive compartments (Fig. 3B, D). Productive genome entry, monitored by the
170 appearance of MeGFP fluorescence at the nuclear margin [11], was apparent 4 h post-inoculation
171 (Fig. 3E) but not 50 min post-inoculation (Fig. 3B). These observations are consistent with the
172 expectation that ZEBOV GP fuses from late endosomes [18,19].
173
174 In the presence of 5 uM apilimod, virions trafficked efficiently to NPC1-positive compartments
175 within 50 minutes (Fig. 3C, D), despite pronounced late endosome and lysosome enlargement,
176 showing that PIKfyve inhibition had not disrupted traffic from the cell surface. At 4 hr post-
177 inoculation, however, the apilimod-treated cells showed no MeGFP signal at the nuclear periphery
178 (Fig. 3F) and failed to support infection (Fig. 3G). That is, PIKfyve inhibition blocked viral genome
179 release from a (swollen) late endosomal compartment, in agreement with our published
180 observations [11]. Infection efficiency decreased with increasing apilimod concentration and
181 endosomal swelling (Fig. 2E, G), further supporting the conclusion that late endosomal
182 enlargement impairs fusion and genome release.
183
184 VSV–SARS-CoV-2 entry can proceed through either a full low-pH and cathepsin-dependent
185 stage, in cells lacking TMPRSS2, or a pathway requiring activation by TMPRSS2 on the cell
186 surface [20–22]. SARS-CoV-2 entry is apilimod sensitive in cells that lack TMPRSS2 (Fig. 1C), but
187 only partially so in cells that express the protease [23] (Fig. 4, 0% hypo). Thus, when TMPRSS2 is
188 present, the virus appears to follow both entry pathways, and fusion can occur either at the plasma
189 membrane or in early endosomes, after TMPRSS2 cleavage, or alternatively in acidic late
190 endosomes, following cathepsin activation.
191

192 We confirmed that apilimod does not inhibit infection by VSV–eGFP–G (Fig.1B) and correlated
193 its resistance with entry from early endosomes. We monitored fusion and cytosolic release, using
194 VSV–eGFP–P–G. Expression of eGFP fused to the viral phosphoprotein (P) allowed us to
195 discriminate between fluorescent virions within NPC1-tagged endosomes and those whose
196 genome was released into the cytosol. SVG-A NPC1-Halo–expressing cells were pulse-
197 inoculated and imaged by LLSM at 30- and 40-minutes post-inoculation, with or without 5 uM
198 apilimod (Fig. 5A–C). After 30 min and in both conditions, 8–96 virions per cell had trafficked to
199 NPC1-positive compartments, and ~20% of P-spots associated with the viral genome had been
200 released into the cytosol (Fig. 5D–F). These results indicate that genome release occurs in early
201 endosomes, with a subset of virions becoming trapped in late endosomes. The similar fraction of
202 cytosolic particles in apilimod-treated and untreated cells is consistent with the resistance of VSV
203 G–mediated infection to PIKfyve inhibition and agrees with similar results obtained in prior
204 infectivity studies [11].
205
206 **Endosomal swelling by ammonium accumulation, not PI(3,5)P_2 loss, accounts for**
207 **blockage of VSV–MeGFP-ZEBOV infection by PIKfyve inhibitors**
208 Under normal conditions, cytosolic glutamine is converted in mitochondria to NH_3, which enters
209 endosomes and lysosomes, where acidification by the endo-lysosomal V-ATPase traps it as NH_4^+
210 [24]. PIKfyve inhibition induces endo-lysosomal swelling through ammonium accumulation and
211 water influx, an effect prevented by glutamine withdrawal from the medium [24] or by inhibition of
212 the V-ATPase [25]. We took advantage of this relationship to distinguish between a biochemical
213 consequence of PI(3,5)P_2 depletion by acute apilimod treatment from a broader physical block to
214 infection caused by endosomal swelling, by testing whether the blockade of infection could be
215 reversed by limiting ammonium accumulation.
216
217 To validate our experimental system, we imaged SVG-A cells in FluoroBrite medium containing
218 apilimod, with or without supplementation with 4 mM glutamine and FBS. Late endosomes and
219 lysosomes were labeled with internalized Dextran-568 (Fig. 6A). As expected, apilimod-induced
220 endosomal swelling, visually monitored for up to 30 min, was markedly reduced in glutamine-free
221 medium (Fig. 6B). Based on this observation, we inoculated cells for 30 min with VSV-MeGFP-
222 ZEBOV in standard buffer (e.g. containing glutamine), followed by a 30 min incubation with
223 apilimod in the presence or absence of glutamine. Glutamine and 50 nM apilimod were then
224 added for the remainder of the assay to restrict the test of viral entry to the 30 min post-inoculation
225 window, comparing the effect with and without glutamine (Fig. 6C). This step was necessary

226 because prolonged incubation in glutamine-free medium during early infection blocked synthesis
227 of MeGFP encoded by VSV-MeGFP–ZEBOV. VSV-MeGFP–ZEBOV infection was reduced by
228 ~60% in the presence of both glutamine and apilimod but was minimally affected in glutamine-
229 free medium with apilimod (Fig. 6C–E). These results suggest that inhibition of infection arises
230 from endosomal swelling itself, rather than from loss of PI(3,5)P_2-dependent signaling.
231
232 **Hypotonic-induced endolysosomal swelling reduces VSV-MeGFP–ZEBOV and VSV-eGFP–**
233 **SARS-CoV-2 infection**
234 To test directly whether endolysosomal osmotic swelling impairs viral entry, we used a non-
235 pharmacological method to enlarge endosomes and lysosomes during the early phase of
236 infection. Brief incubation of cells in hypotonic medium induces transient swelling of the cytoplasm
237 and intracellular membrane-bound compartments, most prominently late endosomes and
238 lysosomes [26–28]. We exploited this osmotic effect to perturb the entry process of VSV-eGFP-G,
239 VSV-MeGFP–ZEBOV and VSV-eGFP–SARS-CoV-2. A single 30-minute hypotonic pulse,
240 initiated 30 minutes post-inoculation, was reversible, did not lead to cell death and targeted the
241 entry window while minimizing artifacts from subsequent volume regulation.
242
243 To quantify endosomal swelling, we incubated Vero cells in medium diluted with increasing
244 amounts of water and measured endolysosomal size by spinning-disk confocal imaging of cells
245 preloaded with Alexa Fluor 568–labeled dextran (Dextran-AF568; Fig. 7A). Using the same 90th
246 percentile radius cutoff (0.73 μm) as in the apilimod experiments, we observed a modest increase
247 in enlarged compartments with 30% dilution and a robust increase with 60% dilution, whereas
248 10% dilution had no detectable effect (Fig. 7B–D).
249
250 We next tested the impact of this hypotonic swelling on infection. SVG-A or Vero cells were
251 inoculated with VSV-MeGFP–ZEBOV, VSV-eGFP–SARS-CoV-2, or VSV-eGFP-G, then
252 subjected to 30-minute hypotonic treatments at the indicated dilutions (Figs. 7E-G and 8). To
253 restrict continued viral fusion after the swelling phase, we added Bafilomycin A1 alone (VSV-G),
254 apilimod alone (VSV-MeGFP-ZEBOV) or in combination with apilimod (VAV-SARS-CoV-2)
255 immediately following the hypotonic pulse. Bafilomycin A1 blocks endosomal acidification [29] and
256 thereby prevents low pH-dependent viral membrane fusion. The combination of Bafilomycin A1
257 and apilimod inhibited fusion of VSV-MeGFP–ZEBOV and VSV-eGFP–SARS-CoV-2. Infection of
258 SVG-A cells by VSV-MeGFP–ZEBOV dropped to ~40% of control levels following 60% dilution,
259 with no inhibition at lower dilutions (Fig. 7F and G). The same treatment in Vero cells suppressed

260 infection by ~ 50% for both VSV-eGFP–SARS-CoV-2 and VSV-MeGFP–ZEBOV but had no effect
261 on VSV-eGFP (Figs. 8B-D). The similarity between these results and those obtained with apilimod
262 supports the conclusion that late endosomal swelling mediated by transient hypotonicity rather
263 than inhibition of a specific biochemical pathway selectively blocks infection by viruses that require
264 trafficking to late endosomes, preventing membrane fusion and cytosolic genome delivery.
265
266 To test whether hypotonic treatment inhibits infection primarily through late endosomal swelling,
267 we took advantage of the differential activation of SARS-CoV-2 spike (S): TMPRSS2 activates S
268 at the cell surface/early endosomes, whereas cathepsins do so in late endosomes [20–22]. In Vero
269 cells ectopically expressing TMPRSS2, concurrent treatment with camostat (a TMPRSS2 inhibitor
270 that prevents early entry) and apilimod (which blocks late entry) completely inhibited VSV-SARS-
271 CoV-2 infection (Fig. 4A–C) [23]. Either compound alone caused the expected partial inhibition
272 (~60% for apilimod, ~25% for camostat) consistent with additive effects on distinct entry routes
273 (Fig. 4C) [23].
274
275 If hypotonic swelling acts primarily in late endosomes, infection should be strongly inhibited when
276 TMPRSS2 is absent or blocked by camostat, and only weakly inhibited when TMPRSS2 is active.
277 Our results matched these predictions: 60% hypotonic treatment inhibited infection by 50-60%
278 either without TMPRSS2 (Fig. 7D) or with TMPRSS2 plus camostat (Fig. 4C), but only by ~20%
279 when TMPRSS2 was present without camostat (Fig. 4C). Consistent with late-endosomal fusion,
280 combining hypotonic treatment with apilimod did not further reduce infection (~60%, Fig. 4C).
281 Conversely, by preventing early entry, camostat sensitized infection to hypotonic swelling (~20%
282 without vs ~ 60% with camostat, Fig. 4C). Together, these results support our inference that
283 hypotonic swelling blocks infection by interfering with the late endosomal entry pathway.
284
285 **Free and membrane-bound VSV-MeGFP–ZEBOV virions in swollen endosomes**
286 Finally, we assessed whether VSV-MeGFP–ZEBOV virions remain membrane-bound under
287 swelling conditions that block infection using 3D live-cell LLSM imaging of virions within apilimod-
288 induced, enlarged NPC-1-Halo containing late endosomes and lysosomes in SVG-A cells (Figs.
289 3C, F and 9). We did not use hypotonic swelling because both transience and heterogeneity limit
290 resolution and stability during live-cell imaging. In non-swollen endosomes (~300-500 nm
291 diameter), the point-spread function of the microscope precludes distinguishing virions at the
292 limiting membrane from those in the lumen (Figs. 3B, E). In contrast, apilimod-induced swelling
293 yields larger endosomes of ~1 µm diameter (Figs. 3C, F), enabling spatial separation of

294 membrane-bound and luminal particles (Figs. 3C, F and 9). Because these compartments remain
295 acidic [10], we expected most virions to remain receptor-bound and fusion-competent.
296
297 We used 3D live-cell LLSM to quantify the movement of fluorescent virions inside swollen
298 compartments labeled with endogenously tagged NPC1-Halo (Fig. 9). Treatment with 5 μM
299 apilimod produced largely immobile enlarged endosomes, in contrast to the dynamic trafficking
300 observed in untreated cells. Visual inspection of z-projected 3D time series revealed that ~75%
301 of 859 fluorescent VSV-MeGFP–ZEBOV virions localized to the lumen while the 25% remainder
302 colocalized with the limiting membrane (Fig. 9B, C, F). A similar distribution of virions in the lumen
303 was also observed for VSV-P-eGFP-G, which is not sensitive to apilimod treatment (Fig. 9F). In
304 that case, ~75% of 590 virions remained membrane bound while the rest were in the lumen.
305 These observations were unexpected.
306
307 To distinguish luminal from membrane-associated behavior, we tracked the 3D positions of
308 individual VSV-MeGFP–ZEBOV particles over time in SVG-A cells. Using time-resolved LLSM at
309 4-second intervals, we followed fluorescent virions within swollen compartments and computed
310 their mean squared displacement (MSD) (representative examples depicted in the insets in Fig.
311 9). Particles localized to the lumen had nearly constant MSD values (Fig. 9B), consistent with the
312 confinement within a spherical volume, as expected from a plateau value of 3/5 R^2 (Fig. 9D). In
313 contrast, particles stably associated with the limiting membrane showed constrained motion and
314 MSD profiles consistent with movement of the surface of a rotating sphere (Fig. 9C, E). Variation
315 in particle and compartment dynamics resulted in diverse trajectory patterns. We restricted this
316 analysis to representative examples, as current computational limitations precluded automated
317 processing of larger datasets.
318
319 We interpret these single-virion imaging results as follows. In normal acidic endosomes, VSV-
320 eGFP-P-G and VSV-MeGFP–ZEBOV remain stably associated with their respective receptors.
321 VSV-G–mediated fusion occurs primarily in early endosomes, which are not subject to osmotic
322 swelling. Because NPC1 is absent from this compartment, VSV-MeGFP–ZEBOV fusion does not
323 occur there. As VSV-eGFP-P-G and VSV-MeGFP–ZEBOV virions traffic further, arrival in swollen
324 late endosomes correlates with a loss of stable membrane association. We attribute this shift to
325 increased membrane tension, which could impede viral fusion by raising the energetic barrier to
326 the membrane deformations required for hemifusion and full fusion. Alternatively, in the acidic
327 environment of swollen endosomes, unbound viral glycoproteins that have not yet engaged the

328 limiting membrane may undergo a premature low pH–induced conformational change, thus
329 making them unable to rebind and no longer capable of driving fusion. This mechanism would
330 explain both the retention of virions at the membrane and the release of others into the lumen,
331 where they become fusion-incompetent and unable to rebind. For VSV-G, this has little
332 consequence, as fusion typically occurs in the early endosome, e.g. upstream of this
333 compartment. In contrast, for VSV-MeGFP-ZEBOV, the combination of altered membrane
334 mechanics and disrupted NPC1 engagement in late endosomes likely underlies the observed
335 failure to fuse and the consequent block in infection.

336 **DISCUSSION**

337 We examined why inhibition of the endosomal lipid kinase PIKfyve selectively blocks infection by
338 certain membrane-enveloped viruses, represented here by VSV chimeras bearing the SARS-
339 CoV-2 spike or Ebola virus GP, while leaving parental VSV-G–mediated infection unaffected.
340 Using a combination of quantitative infectivity assays and high-precision, live-cell 3D imaging, we
341 identified a previously unrecognized and mechanistically simple explanation: endosomal
342 membrane swelling acts as a biophysical barrier to viral fusion and genome delivery into the
343 cytosol.
344
345 Previous models have attributed the antiviral effects of PIKfyve inhibition primarily to disruptions
346 in endosomal maturation or impaired trafficking of virions to protease-rich, fusion-competent
347 compartments. While consistent with the dependence of SARS-CoV-2 and Ebola virus on late
348 endosomal cathepsin activity and NPC1 function, these models do not account for our earlier
349 observations by live-cell single virion fluorescence microscopy, confirmed here, that these virions
350 trafficked normally to the swollen NPC1-positive compartments under PIKfyve inhibition but failed
351 to initiate productive infection.
352
353 Our findings uncouple PI(3,5)P_2 depletion from the block in viral infection. Although apilimod
354 inhibits PIKfyve and reduces PI(3,5)P_2 levels, the antiviral effect against VSV-SARS-CoV-2 and
355 VSV-ZEBOV requires endosomal swelling, a process driven by glutamine-dependent
356 accumulation of NH_4^+ and consequent osmotic influx. Apilimod treatment in glutamine-depleted
357 media failed to block infection, indicating that PI(3,5)P_2 loss alone is insufficient to impair viral
358 entry. Furthermore, apilimod treatment slightly decreases endolysosomal pH [30,31]. These
359 observations implicate a mechanical disruption of the fusion-permissive environment, rather than
360 defects in endosomal acidification. Thus, the antiviral activity of apilimod depends on a biophysical
361 alteration of endosomal membranes rather than solely on phosphoinositide depletion.
362
363 We further demonstrated that transient hypotonic late endosome swelling, in the absence of
364 PIKfyve inhibition, phenocopies the antiviral effect, reinforcing our conclusion that osmotic
365 expansion of endosomal volume rather than disruption of lipid signaling impairs viral entry.
366 These observations together with our observation that apilimod did not hinder the traffic of VSV-
367 G, VSV-ZEBOV or VSV-SARS-CoV2 to the endolysosomal compartment (this study and see
368 also [11]) strengthen the conclusion that the key barrier is not trafficking or maturation failure, but
369 instead a tension-induced mechanical resistance of the endosomal membrane to the

370 deformation required for fusion and pore formation. Fusion requires precise spatial coordination
371 between viral and host membranes, and a membrane environment permissive for local
372 deformation. Swollen endosomes may resist the bending and curvature of the limiting
373 membrane necessary for pore formation, particularly for glycoproteins with stringent
374 conformational checkpoints, such as VSV G, EBOV GP, or SARS-CoV-2 spike.
375
376 Why is infection by VSV-G unaffected by apilimod treatment or osmotic swelling? The simplest
377 explanation is that VSV-G–mediated fusion and genome release occur in early endosomes,
378 which are not subject to PIKfyve-dependent swelling. Indeed, previous studies using dominant-
379 negative Rab GTPase mutants showed that VSV infection is inhibited by Rab5(S34N), but not
380 by Rab7(T22N), indicating that fusion occurs before endosomal maturation into Rab7-positive
381 compartments [32–34]. Inhibition of PIKfyve kinase also has a minimal effect on influenza-virus
382 infection [16], and evidence from use of dominant-negative Rab 5 and 7 GTPase mutants
383 indicates that influenza-virus fusion occurs in in both early and late endosomes [34]. Our
384 proposed mechanism for apilimod resistance is further supported by our finding that apilimod-
385 mediated inhibition of VSV-SARS-CoV-2 infection is only partial in cells expressing TMPRSS2
386 and only becomes complete in its absence (this study, see also [23]). TMPRSS2-mediated
387 activation of the SARS-CoV-2 spike promotes fusion at the plasma membrane or within early
388 endosomes, bypassing the late endosomal route [20–22]. Accordingly, in TMPRSS2-negative cells
389 where both VSV-SARS-CoV-2 and VSV-ZEBOV rely on late endosomal fusion, the extent of
390 inhibition by osmotic challenge is similar. Thus, viral fusion is governed not solely by pH or
391 receptor engagement but also by the trafficking itinerary of the virion and the mechanical state
392 of the endosomal membrane at the site of fusion.
393
394 Many enveloped viruses, including filoviruses, coronaviruses, and arenaviruses rely on late
395 endosomal or lysosomal compartments for entry (see review [35]), making them potentially
396 sensitive to perturbations in membrane mechanics. Targeting host pathways that regulate
397 endosomal membrane tension, such as PIKfyve or its lipid effectors, offers a mechanistically
398 distinct antiviral strategy, one that does not interfere with receptor binding or protease activation,
399 but instead acts at the level of fusion competence. By identifying membrane tension as a key
400 regulator of viral entry, our study highlights the utility of integrating biophysical parameters into
401 models of intracellular viral trafficking and fusion.

402 **MATERIAL AND METHODS**

403 **Reagents**

404 The following reagents were used: apilimod (HY-14644, MedChemExpress), Bafilomycin A1
405 (B1793-2UG, Sigma-Aldrich), Milli-Q water (Z00QSV0US, MilliporeSigma), Minimum Essential
406 Medium (MEM; 10-010-CV, Corning), Dulbecco's Modified Eagle Medium (DMEM; 10-013-CV,
407 Corning), penicillin-streptomycin (45000-652, VWR), fetal bovine serum (S11150H, Atlanta
408 Biologicals), Alexa Fluor 568 dextran-10K (D-22912, Invitrogen), Janelia Hoechst 646 and Janelia
409 Fluor 646 HaloTag ligand (gifts from Luke Lavis, Janelia Research Campus, HHMI), FluoroBrite
410 DMEM (A1896701, Gibco), HEPES buffer (SH30237.01, Cytiva), and paraformaldehyde (P6148,
411 Sigma-Aldrich).

412

413 **Cell Culture**

414 VeroE6-TMPRSS2 cells (a gift from Siyan Ding [36]) and Vero C1008 cells (Vero 76, clone E6;
415 ATCC CRL-1586) were maintained in DMEM supplemented with 10% fetal bovine serum (FBS)
416 and 1% penicillin-streptomycin (P/S) at 37°C in 5% CO_2. SVG-A cells (ATCC CRL-8621) and a
417 homozygous gene-edited derivative expressing EEA1–mScarlet and NPC1–HaloTag from both
418 alleles [11] were cultured in MEM with 10% FBS and 1% P/S under the same conditions. All
419 experiments used cells passaged fewer than 10 times. Cultures were routinely tested and
420 confirmed negative for mycoplasma.

421

422 **Production and Propagation of Chimeric Vesicular Stomatitis Viruses**

423 Recombinant vesicular stomatitis viruses (VSVs) encoding fluorescent reporters and distinct
424 glycoproteins were used. VSV-eGFP-G expresses enhanced GFP (eGFP) and retains the native
425 VSV glycoprotein G [37]. VSV-eGFP-P-G expresses eGFP fused to the viral phosphoprotein (P) [11],
426 a cofactor that associates with the large (L) polymerase protein within the virion and is required
427 for efficient RNA-dependent RNA synthesis from the ribonucleoprotein (RNP) template. Each
428 virion contains approximately 165 copies of P [38]. In VSV-eGFP–SARS-CoV-2, glycoprotein G is
429 replaced by the SARS-CoV-2 spike (S) protein (Wuhan-Hu-1) [39]. VSV-MeGFP-ZEBOV encodes
430 the Zaire ebolavirus (ZEBOV) glycoprotein in place of G and expresses eGFP fused to the matrix
431 (M) protein [40]. We estimate that each virion contains ~1200 MeGFP molecules, assuming the
432 number of MeGFP copies approximates that of the M protein in VSV [41].

433

434 Chimeric viruses were propagated in confluent Vero E6 monolayers plated in 15 cm dishes.
435 Growth medium (DMEM with 10% FBS) was removed, and cells were rinsed once with DMEM

436 containing 1% P/S to remove residual serum. Cells were infected at a multiplicity of infection (MOI)
437 of ~0.01 in 10 mL DMEM supplemented with 0.4% FBS and 1% P/S and incubated for 48 h at
438 37°C, 5% CO_2. Supernatants were collected, clarified by centrifugation at 3580 rpm for 10 min at
439 4°C (Beckman Coulter GS-6KR), and divided into two portions: one was stored at 4°C for up to
440 one week for titration and infection assays; the other was aliquoted (0.5 mL), flash-frozen in liquid
441 nitrogen, and stored at −80°C for imaging-based experiments.
442
443 **Virus infection**
444 Viral supernatant (100 µL) was diluted in serum-free DMEM containing 1% P/S and applied to
445 cells plated in 48-well plates (82051-004, VWR) for 30 min at 37°C. Unbound virus was removed
446 by three washes with DMEM supplemented with 10% FBS and 1% P/S. Cells were then incubated
447 in fresh complete medium for 8 h at 37°C in 5% CO_2. Fixation was performed with 4%
448 paraformaldehyde (PFA) in PBS for 15 min at room temperature. The multiplicity of infection (MOI)
449 was estimated by quantifying eGFP-positive cells relative to the total population (see Infection
450 Analysis). The 16% (w/v) stock PFA solution was prepared by dissolving 16 g of PFA powder
451 (P6148, Sigma-Aldrich) in 80 mL of preheated 1× PBS (60°C) with stirring for 10 min. We added
452 drops of 10 N NaOH (221465, Sigma-Aldrich) every 5 min until the suspension cleared. After
453 cooling to room temperature, we filtered the solution through a grade 1 Whatman™ filter (09-805-
454 1G, Cytiva), adjusted the pH to 7.2 using a calibrated pH meter (Hi 2211, Hanna Instruments),
455 and aliquoted it into 10 mL portions for storage at −20°C.
456
457 **Apilimod Treatment and Infection**
458 Vero E6 cells were seeded at 35–40% confluency in sterile 48-well plates (82051-004, VWR) and
459 used the following day. Cells were pretreated for 1 h at 37°C with 0.1% dimethyl sulfoxide (DMSO;
460 vehicle control) or with 0.01, 0.05, or 5 µM apilimod in DMEM supplemented with 10% FBS and
461 1% P/S. After pretreatment, cells were inoculated with the indicated chimeric virus for 30 min in
462 serum-free DMEM containing 1% P/S and the corresponding concentration of DMSO or apilimod.
463 Unbound virus was removed by three washes with DMEM containing 10% FBS and 1% P/S,
464 followed by incubation for 7 h at 37°C in 5% CO_2. Cells were then washed three times with PBS
465 (0.5 mL) and fixed with 4% PFA in PBS for 15 min at room temperature. Nuclei were labeled by
466 incubation with 100 nM Janelia Hoechst 646 in PBS for 1 h at room temperature. Imaging was
467 performed without washing out the dye.
468
469 **Hypotonic treatment and Infection**

470 Hypotonic media were prepared by diluting complete MEM or DMEM with sterile Milli-Q water:
471 10% (1 mL water + 9 mL medium), 30% (3 mL water + 7 mL medium), and 60% (6 mL water + 4
472 mL medium).
473
474 SVG-A or Vero E6 cells were seeded at 35–40% confluency in 48-well plates and used the
475 following day. Cells were infected VSV-eGFP–SARS-CoV-2 or VSV-MeGFP-ZEBOV at an MOI
476 of ~0.5 for 30 min in 200 µL of serum-free MEM for SVG-A or DMEM for Vero E6, each
477 supplemented with 1% P/S, at 37°C and 5% CO_2. Unbound virus was removed by three washes
478 with complete medium (MEM or DMEM supplemented with 10% FBS and 1% P/S, 0.5 mL per
479 wash). Infection was then either blocked by adding 100 nM bafilomycin A1 (VSV-eGFP) or 5 µM
480 apilimod (VSV-eGFP–SARS-CoV-2 and VSV-MeGFP-ZEBOV), and allowed to proceed in
481 corresponding serum-free or hypotonic media for 30 min at 37°C. Cells were then returned to
482 complete medium (10% FBS, 1% P/S) and incubated for 7 h at 37°C in 5% CO_2.
483
484 Vero cells stably expressing TMPRSS2 were seeded at 35–40% confluency in sterile 48-well
485 plates (82051-004, VWR) and used the next day. Cells were pretreated for 1 h at 37°C in 5%
486 CO_2 with 0.1% DMSO (vehicle) alone or with 5 µM apilimod, 5 µM camostat, or both in DMEM
487 supplemented with 10% FBS and 1% P/S. Following pretreatment, cells were infected with
488 VSV-eGFP-SARS-CoV-2 (MOI ~0.5) in 200 µL serum-free DMEM (1% P/S) containing the
489 same inhibitor conditions. After 30 min at 37°C, unbound virus was removed by three washes
490 with complete DMEM (10% FBS, 1% P/S; 0.5 mL/wash). Infection was then allowed to proceed
491 for 30 min in 60% hypotonic medium containing 0.1% DMSO alone or with 5 µM apilimod, 5 µM
492 camostat, or both. Cells were subsequently returned to complete DMEM containing the same
493 inhibitor conditions to prevent further infection and incubated for 7 h at 37°C in 5% CO_2.
494
495 The experiment ended by washing the cells three times with PBS (0.5 mL), fixing with 4% PFA
496 in PBS for 15 min at room temperature, and staining with 500 nM Janelia Hoechst 646 in PBS
497 for 1 h before imaging.
498
499 **Glutamine Deficiency and Infection**
500 SVG-A cells were seeded at 35–40% confluency in sterile 48-well plates (82051-004, VWR) and
501 used the next day. Cells were infected with the VSV-MeGFP-ZEBOV chimeric virus (MOI ~0.5)
502 for 30 min in serum-free DMEM (including 4 mM glutamine) supplemented with 1% P/S. Unbound
503 virus was removed by three washes with FluoroBrite DMEM supplemented with 10% FBS, 1%

504 P/S (glutamine-free) or DMEM (including 4 mM glutamine) supplemented with 10% FBS and 1%
505 P/S . The cells were incubated in FluoroBrite DMEM (glutamine-free, 10% FBS, 1% P/S) or DMEM
506 (4 mM glutamine,10% FBS, 1% P/S) containing either 0.1% DMSO or 50 nM apilimod for 30 min
507 at 37°C. After three washes with DMEM (including 4 mM glutamine) supplemented with 10% FBS
508 and 1% P/S, cells were incubated for 7 h at 37°C in 5% CO_2, then washed three times with PBS
509 (0.5 mL) and fixed with 4% PFA in PBS for 15 min at room temperature. Nuclei were then labeled
510 by incubating cells with 100 nM Hoechst Janelia 646 in PBS for 1 h at room temperature. Imaging
511 was performed without washing out Hoechst Janelia 646 dye.
512
513 **Apilimod, Glutamine, and Hypotonic Treatments and Endolysosomal Size**
514 Vero E6 cells were seeded at 35–40% confluency in 8-well glass-bottom chambers (C8-1.5H-N,
515 Cellvis) and imaged the following day. Endolysosomes were labeled by incubating cells with 10
516 μM Alexa Fluor 568–dextran in DMEM supplemented with 10% FBS and 1% P/S for 2 h at 37°C
517 in 5% CO_2. Apilimod (final concentration of 0.01, 0.05 or 5 μM in 0.1 % DMSO) was added for 1
518 h before and then during the Dextran uptake period, after which cells were washed three times
519 with complete DMEM media (supplemented with 10% FBS and 1% P/S) to remove extracellular
520 dye, followed by live cell imaging in FluoroBrite DMEM supplemented with 5% FBS, 1% P/S, and
521 25 mM HEPES (pH 7.2) including apilimod at the indicated concentrations. Experimental
522 conditions were initiated in 15-minute intervals across the 8-well chamber. Each well was imaged
523 for 10 minutes before applying the same washing and medium exchange protocol to the next well.
524
525 To study the effect of glutamine removal on apilimod induced endolysosome expansion, SVG-A
526 cells were seeded at 35-40% confluency in 8-well glass bottom chambers (C8-1.5H-N, Cellvis)
527 for the following day. Endolysosomes were pre-labeled with 10 μM Alexa Fluor 568–dextran in
528 DMEM supplemented with 10% FBS and 1% P/S for 2 h at 37°C in 5% CO_2. Prior imaging, media
529 was replaced with 50 nM of apilimod in FluoroBrite DMEM supplemented with 10% FBS, 1% P/S
530 (glutamine-free) or DMEM supplemented with 10% FBS and 1% P/S, (including 4 mM glutamine).
531 and timelapse images were acquired in lattice light sheet microscopy to record apilimod induced
532 expansion of dextran labeled compartments.
533
534 For osmotic expansion assays, we replaced the imaging medium with hypotonic solutions (10%,
535 30%, or 60%) and immediately initiated live-cell imaging on a spinning disk confocal microscope
536 at 2-minute intervals for 30 minutes.
537

538 **Virus Tracking**

539 Gene-edited SVG-A cells expressing EEA1–mScarlet and NPC1–HaloTag chimeras instead of
540 the native proteins were seeded at 35–40% confluency in 8-well glass-bottom chambers and
541 imaged the following day. NPC1 compartments were labeled by incubating cells with 500 nM
542 Janelia Fluor 646 HaloTag ligand (JFX 646) in MEM supplemented with 10% FBS and 1% P/S
543 for 15 min at 37°C, followed by three washes with the same medium.

544

545 Cells were then pretreated for 1 h with 0.1% DMSO (vehicle) or 5 μM apilimod in complete MEM.
546 After pretreatment, cells were incubated with the indicated virus in the same medium for 10 min
547 at 37°C, washed three times, and returned to fresh medium containing the same drug conditions
548 for an additional 50 min. Live 3D imaging was performed using a lattice light-sheet microscope in
549 FluoroBrite DMEM supplemented with 5% FBS, 1% P/S, 25 mM HEPES (pH 7.2), 0.1% DMSO,
550 and 5 μM apilimod.

551

552 **Fluorescence Microscopy**

553 **Imaging of Fixed Samples to Assess Primary Infection**

554 Fixed-cell imaging was performed using a Zeiss Axiovert 200M inverted microscope (Carl Zeiss)
555 equipped with a CSU-22 spinning disk confocal unit (Yokogawa) and controlled by the Marianas
556 imaging platform (3i, Intelligent Imaging Innovations). A 10× objective with a 2× magnifier was
557 used. Samples were excited with 491 nm and 660 nm solid-state lasers (50 mW each), and
558 fluorescence was detected using 525/50 and 680LP emission filters (Semrock), respectively.

559

560 Z-stacks (12 optical sections at 3 μm intervals) were acquired with a piezoelectric Z-stage (PZ-
561 2000) and encoded XY stage (MS-2000, Applied Scientific Instruments). Images were captured
562 at 50% laser power (0.68 mW at the back aperture) with 200 ms exposure per plane using a
563 QuantEM 512SC air-cooled CCD camera (Photometrics).

564

565 **Live-Cell 3D Imaging of Endosomes and Lysosomes**

566 Live imaging was performed using a Zeiss Axio Observer Z1 inverted microscope equipped with
567 environmental control (37°C, 5% CO_2) and a CSU-X1 spinning disk confocal unit (Yokogawa),
568 operated via the Marianas (3i) platform. The system included a spherical aberration correction
569 module and a 3i LaserStack with diode lasers at 488, 560 (150 mW), and 640 nm (100 mW).
570 Emission was filtered using 525/40, 609/54, and 692/40 filters (Semrock).

571

572 Z-stacks comprising 75 optical planes at 0.270 µm spacing were acquired with 20 ms exposure
573 per plane using a dual-camera sCMOS system (Prime 95B, Teledyne Photometrics). A custom
574 bandpass dichroic (Semrock; transmit 350–560 nm and 641–800 nm, reflect 561–640 nm)
575 enabled simultaneous multichannel imaging. Final XY resolution was 0.145 × 0.145 µm/pixel.
576
577 **Live-Cell 3D Lattice Light Sheet Microscopy for Virus Tracking**
578 Lattice light sheet imaging was performed using a Zeiss Lattice Lightsheet 7 system with a
579 dithered lattice beam (30 µm × 0.7 µm). Cells were maintained at 37°C in a humidified chamber
580 with 5% CO_2. Illumination was provided by 488 nm (10 mW, 2 mW at pupil), 561 nm (10 mW, 2
581 mW), or 640 nm (5 mW, 1 mW) lasers, typically operated at 1–1.5% power.
582
583 A 13.3×, NA 0.4 objective (Zeiss) was used for illumination, and a 44.83×, NA 1.0 objective (Zeiss)
584 for detection. Z-stacks were acquired using sample scanning with 0.25 µm optical sectioning and
585 0.5 µm axial spacing. Each plane was captured with a 5 ms exposure using dual ORCA-Fusion
586 sCMOS cameras (Hamamatsu), yielding a final XY resolution of 0.145 × 0.145 µm/pixel.
587
588 Time-lapse imaging was performed at 3 s intervals for virus tracking and at 3 min intervals for
589 apilimod-induced endosome and lysosome expansion, over durations of 5–45 min. Raw image
590 stacks were deskewed using ZEISS ZEN 3.11 software prior to analysis.
591
592 **Image Analysis**
593 ***Infectivity assay***
594 Z-stacks (12 optical sections) were acquired at 20× magnification to capture cytosolic eGFP signal
595 from infected cells and nuclear staining with Hoechst 646, imaged 8 h post-inoculation (see
596 Fluorescence Microscopy). This protocol ensured that the signal reflected a single round of
597 infection [11]. Maximum intensity projections were generated using FIJI. Nuclear segmentation was
598 performed using the LabKit plugin in FIJI [42] to determine the number of cells per field and to
599 generate nuclear masks for infection scoring.
600
601 A cell was classified as infected if the eGFP signal within the nuclear mask (z-maximum
602 projection) exceeded a threshold defined by the signal in the eGFP channel from uninfected
603 control samples. The percentage of infected cells was calculated as the number of eGFP-positive
604 nuclei relative to the total number of segmented nuclei, using a custom FIJI script. Results were

605 validated by visual inspection of a representative subset. A minimum of 16,000 cells per condition
606 were analyzed, derived from three independent experiments, each performed in triplicate.
607
608 **Colocalization Between NPC1–Halo–Labeled Compartments and Fluorescently Tagged**
609 **Virions**
610 Z-stacks from single-timepoint live-cell 3D lattice light sheet images of cells inoculated with M–
611 eGFP–tagged virions were used to assess colocalization with NPC1–Halo–labeled
612 endolysosomal compartments. Virus particles, detected as diffraction-limited spots, were
613 identified using the MATLAB-based 3D CME Analysis software [43]. For each virion, mean
614 fluorescence intensity in the NPC1–Halo channel was measured in a 3 × 3 × 3 voxel cube
615 centered on the particle. A virion was classified as colocalized if the NPC1–Halo signal within this
616 volume exceeded the background signal measured in a cytosolic region devoid of NPC1–Halo
617 signal. Analysis was automated using a custom MATLAB script and manually validated in FIJI.
618
619 **Measurement of Endosome and Lysosome Radii**
620 Endosomes and lysosomes labeled with Alexa Fluor 568–dextran internalized for [xx] h were
621 imaged volumetrically using 3D live-cell spinning disk confocal microscopy. Centroid positions of
622 labeled compartments were identified using the 3D CME Analysis software [43]. At the z-plane
623 corresponding to each centroid, radial intensity profiles were calculated in the XY plane by
624 measuring the distance from the centroid to the point at which fluorescence intensity declined to
625 30% of the peak value. Measurements were taken in 2° increments over 360° (180 measurements
626 per compartment), and the mean radial distance was reported as the organelle radius.
627
628 **3D Tracking of Virions Within NPC1–Halo–Labeled Endolysosomes**
629 Live-cell 3D time-lapse datasets acquired using lattice light sheet microscopy were used to track
630 the motion of M–eGFP–tagged virions within apilimod-induced swollen endolysosomes labeled
631 with NPC1–Halo. The centroid and fluorescence intensity of each diffraction-limited virion were
632 determined at each time point using the 3D CME Analysis software [43]. Virion trajectories were
633 assembled by linking detections across frames based on two criteria:
634
635 (i) The virion remained within a 3D spatial window centered on an NPC1–Halo–positive
636 endolysosome, defined in XY as a 25 × 25-pixel region (~2.5 × 2.5 μm), centered on the centroid
637 position of the compartment identified using the Multi-Template Matching plugin in FIJI [44] . The Z-

position of the endolysosome centroid was assigned as the plane of maximal NPC1–Halo signal within ±4 z-planes.

(ii) The virion's fluorescence intensity varied by no more than ± 30% between consecutive time points.

Confinement of a trajectory within a given endolysosome was validated by visual inspection in FIJI, using maximum intensity projections overlaid with bounding boxes centered on the XY coordinates of the NPC1–Halo signal.

Mean square displacement (MSD) analysis of the time-dependent 3D centroid positions was used to distinguish between confined and bound motility behaviors.

Statistical Analysis

Statistical comparisons between control and experimental groups were performed using one-way ANOVA (parametric). Significance levels are indicated by asterisks: *$p < 0.05$; **$p < 0.01$; ***$p < 0.001$; ****$p < 0.0001$. Comparisons without annotated p-values were not statistically significant.

Materials, Data, and Code Availability

All materials, datasets, and custom analysis code are available upon request. For further information or to request resources and reagents, please contact the lead author at kirchhausen@crystal.harvard.edu.

660 **ACKNOWLEDGMENTS**
661 We thank S.C. Harrison for editorial help, S. Whelan for support, M. Cornejo Pontelli for
662 generously providing stocks of VSV chimeras used in this study, E. Sitarksa for imaging the
663 samples used for the endolysosome enlargement assay, B. Zuniga for assistance with
664 determination of virus concentration, and members of the Kirchhausen laboratory for support
665 and encouragement. We also acknowledge the L. Lavis lab and the Open the Chemistry team
666 (Janelia Research Campus, HHMI) for the generous gift of Hoechst Janelia 646 and Janelia
667 Fluor 646 (JF646) dyes. The research was supported by a National Institute of General Medical
668 Sciences Maximizing Investigators' Research Award GM130386 to T. Kirchhausen and
669 AI163019-05 NIH/NIAID Grant Award to S. Whelan and T. Kirchhausen.
670
671 The Zeiss Lattice Lightsheet 7 microscope, located in the IID-HSPH BSL-3 Imaging Core
672 established in 2024 at the Harvard Chan School, was acquired with generous funding from the
673 Massachusetts Life Sciences Center to S. Fortune and T. Kirchhausen. Acquisition of the
674 computing hardware including the DGX's GPU-based computers, CPU clusters, fast access
675 memory, archival servers, and workstations that made possible this study was supported by
676 generous grants from the Massachusetts Life Sciences Center to T. Kirchhausen and by an
677 equipment supplement to the National Institute of General Medical Sciences Maximizing
678 Investigators' Research Award GM130386 to T. Kirchhausen. Construction of the server room
679 housing the computing hardware was made possible with generous support from the PCMM
680 Program at Boston Children's Hospital.
681
682 **The authors declare no competing financial interests.**
683
684 **Author contributions:** N. Chow, G. Scanavachi, A. Saminathan and T. Kirchhausen
685 conceptualized and designed the experiments; N. Chow and A. Saminathan carried the cell
686 biological experiments; G. Scanavachi carried the optical image analysis. T. Kirchhausen drafted
687 the manuscript and revised it in close consultation with all co-authors.

688 **FIGURES**

689 **Figure 1. Apilimod inhibits infection by VSV chimeras bearing SARS-CoV-2 or ZEBOV**
690 **glycoproteins, but not by VSV-G.**

691 **(A)** Schematic of the infection assay. Vero cells lacking TMPRSS2 were pretreated with 5 μM
692 Apilimod for 1 h, followed by a 30-min incubation with VSV-eGFP-G, VSV-eGFP–SARS-CoV-2,
693 or VSV-MeGFP–ZEBOV at an approximate MOI of 0.5. in the continued presence of 5 μM
694 apilimod. Unbound virus was removed by three consecutive washes (each containing 5 μM
695 apilimod), and cells were maintained in 5 μM apilimod throughout the experiment. At 7.5 h
696 postinfection, cells were fixed, and infection was quantified as the percentage of eGFP-positive
697 cells relative to total nuclei (Hoechst Janelia 646 stain), using automated image analysis encoded
698 by a script in FIJI.

699 **(B–D)** Representative maximum intensity z-projections (top) show cytosolic eGFP (green) and
700 nuclear Hoechst Janelia 646 (magenta) in cells infected with the indicated chimeras, in the
701 presence or absence of apilimod. Quantification (bottom) shows the percentage of infected cells
702 normalized to the untreated control for each biological replicate (n = 3; shown in distinct colors).
703 Technical triplicates appear as dots of the same color. Approximately 16,000 cells were analyzed
704 per condition. Bars represent mean ± SD. Statistical significance was assessed by unpaired t test;
705 ****$P < 0.0001$. Comparisons with $P > 0.05$ are not shown.

706

707 **Figure 2. Apilimod induces dose-dependent endolysosome enlargement and inhibits VSV-**
708 **MeGFP–ZEBOV infection.**

709 **(A)** Schematic of the endolysosome enlargement assay. Vero cells not expressing TMPRRS2
710 were incubated with 10 μM Alexa Fluor 568–labeled dextran (Dextran-AF568) for 2 h, followed by
711 washes to remove unbound dextran. Cells were then treated with apilimod at the indicated
712 concentrations for 1 h and imaged live during a 30 min period, also in the presence of apilimod,
713 using 3D spinning disk confocal microscopy. Dextran-AF568 was used as a fluid-phase marker
714 of endolysosomes.

715 **(B)** Representative maximum intensity z-projection images showing Dextran-AF568 signal
716 (yellow) in cells treated with 0, 0.01, 0.05, or 5 μM apilimod. Enlarged endolysosomes are evident
717 at higher concentrations. Scale bar, 10 μm.

718 **(C)** Distribution of endolysosome radii in cells treated with increasing concentrations of apilimod.
719 Solid lines represent the mean across all cells per condition; shaded regions denote SD. Cell
720 counts: N = 24 (0 μM), 22 (0.01 μM), 29 (0.05 μM), and 24 (5 μM). The gray shaded rectangular

721 region marks the 90th percentile of endolysosome radii with a radius >0.725 μm in the control
722 group (0 μM apilimod).
723 **(D)** Percentage of endolysosomes with a radius > 0.725 μm, plotted against apilimod
724 concentration. Bars represent mean ± SD. Statistical significance was determined by one-way
725 ANOVA compared to control; ****P < 0.0001.
726 **(E)** Schematic of the infection assay. Vero cells not expressing TMPRRS2 were pretreated with
727 0, 0.005, 0.01, 0.05, or 5 μM apilimod for 1 h, followed by a 30-min infection with VSV-MeGFP–
728 ZEBOV (MOI ~ 0.5) in the continued presence of apilimod. Unbound virus was removed by three
729 washes (each containing apilimod), and cells were maintained in drug for the remainder of the
730 experiment. At 7.5 h postinfection, cells were fixed, and fraction of infected cell was determined
731 by establishing the of cells expressing MeGFP cytosolic fluorescence with respect to the total
732 number of cells identified by nuclear staining (Hoechst Janelia 646). Automated analysis was
733 performed using FIJI.
734 **(F)** Representative maximum intensity z-projections of images obtained 3D spinning disc confocal
735 fluorescence microscopy showing infected cells (MeGFP, green) and nuclei stained by Hoechst
736 Janelia 646 (magenta) for each apilimod concentration. Scale bar, 100 μm.
737 **(G)** Quantification of infection, plotted as the percentage of infected cells normalized to the
738 untreated control. Each biological replicate (n = 3) is shown in a different color; technical triplicates
739 are represented as dots of the same color. Approximately 16,000 cells were analyzed per
740 condition. Bars represent mean ± SD. Statistical significance was determined by one-way
741 ANOVA; ****P < 0.0001.
742
743 **Figure 3. Apilimod does not impair VSV-MeGFP–ZEBOV trafficking to NPC1 compartments**
744 **but blocks cytosolic escape and infection.**
745 **(A)** Schematic of the infection assay. Gene-edited SVG-A cells expressing NPC1-Halo were
746 pretreated with 5 μM apilimod for 1 h, followed by a 10-min incubation with VSV-MeGFP–ZEBOV
747 (MOI ~0.5) in the continued presence of 5 μM apilimod. Unbound virus was removed by three
748 washes (each containing 5 μM apilimod), and cells were maintained in drug for the remainder of
749 the experiment. Live-cell imaging using lattice light-sheet microscopy was performed at 50 min
750 and 4 h postinfection. Volumetric time-lapse series were acquired every 4 s for 10 min.
751 **(B, C)** Representative maximum intensity z-projections from the first frame of volumetric time
752 series acquired at 50 min postinfection in **(B)** absence (control) or presence **(C)** of 5 μM apilimod.
753 NPC1-Halo labeled with JFX 646 is shown in magenta, and VSV-MeGFP–ZEBOV in green. Scale
754 bar, 10 μm.

755 **(D)** Quantification of NPC1-positive compartments colocalizing with VSV-MeGFP–ZEBOV at 50
756 min postinfection. Each point represents a single cell (n = 22 control; n = 46 apilimod-treated).
757 Statistical significance was assessed using an unpaired t test; P > 0.05 was considered not
758 significant and is not shown.
759 **(E, F)** Representative maximum intensity z-projections from 4 h postinfection in **(E)** absence
760 **(**control**)** or presence **(F)** of 5 μM apilimod. NPC1-Halo labeled with JF 646 is shown in magenta,
761 and VSV-MeGFP–ZEBOV in green. Scale bar, 10 μm.
762 **(G)** Quantification of number of cells showing viral entry based on MeGFP signal at the nuclear
763 margin as in panel **(E).** Statistical significance was assessed by unpaired t test; ****P < 0.0001.
764
765 **Figure 4. Hypotonic stress partially inhibits VSV-eGFP–SARS-CoV-2 infection via the late**
766 **endosomal pathway but not early endosome–dependent entry.**
767 **(A**) Schematic of the infection assay. Vero cells stably expressing TMPRSS2 were pretreated for
768 1 h with 5 μM apilimod, 5 μM camostat, both, or DMSO vehicle. Cells were then incubated with
769 VSV-eGFP–SARS-CoV-2 for 30 min (MOI ~ 0.5) in the continued presence of the same treatment
770 solution. Unbound virus was removed by three washes, each containing the same treatment.
771 Cells were subsequently exposed to 0% or 60% hypotonic medium for 30 min. After treatment, 5
772 μM apilimod and 5 μM camostat were maintained in the culture medium for the remainder of the
773 experiment (Post apilimod +/- camostat). At 7.5 h postinfection, cells were fixed, and infection
774 was assessed by quantifying eGFP-positive cells relative to total nuclei (Hoechst Janelia 646
775 stain). Automated analysis was performed using FIJI.
776 **(B)** Representative maximum intensity z-projections show cytosolic eGFP (green) and nuclear
777 Hoechst Janelia 646 (magenta) under the indicated treatment conditions with apilimod or
778 camostat during virion incubation and hypotonic treatment.
779 **(C)** Quantification of infection levels. Data are shown as the percentage of infected cells
780 normalized to untreated control for each biological replicate (n = 3; shown in distinct colors).
781 Technical triplicates are represented as same-colored dots. Approximately 16,000 cells were
782 analyzed per condition. Bars represent mean ± SD. Statistical significance was determined using
783 one-way ANOVA; *P < 0.05, ****P < 0.0001. Comparisons with P > 0.05 are not shown.
784
785 **Figure 5. Cytosolic escape and infection by VSV-eGFP–G are not inhibited by apilimod.**
786 **(A)** Schematic of the infection assay. Gene-edited SVG-A cells expressing NPC1-Halo were
787 pretreated with 5 μM apilimod for 1 h, then incubated with VSV-eGFP–G (MOI ~1) for 10 min in
788 the continued presence of drug. Unbound virus was removed by three washes (each containing

789 5 μM apilimod), and cells were maintained in apilimod for the remainder of the experiment. Live-
790 cell imaging was performed at 30 min postinfection using lattice light-sheet microscopy.
791 Volumetric time-lapse series were acquired every 4 s for 10 min.
792 **(B, C)** Representative maximum intensity projections from the first (30 min) and last (40 min)
793 frames of the time series in the absence **(B)** (control) or presence **(C)** of 5 μM apilimod. NPC1-
794 Halo labeled with JFX 646 is shown in magenta, and VSV-eGFP–G in green. White arrowheads
795 mark virions localized in the cytosol. Scale bar, 10 μm.
796 **(D, E)** Quantification of cytosolic VSV-eGFP–G particles per cell at 30 and 40 min postinfection
797 in **(D)** control and **(E)** apilimod-treated cells. Lines connect values from the same cell at both time
798 points.
799 **(F)** Quantification of the percentage of VSV-eGFP–G particles in the cytosol, with or without
800 apilimod. Statistical significance was assessed by unpaired t test; $P > 0.05$ was considered not
801 significant and is not shown.
802
803 **Figure 6. Glutamine depletion moderates apilimod-induced endolysosome enlargement**
804 **and reduces its antiviral efficacy.**
805 **(A)** Schematic of the live-cell assay. Vero cells not expressing TMPRSS2 were incubated with 10
806 μM Alexa Fluor 568–labeled dextran (Dextran-AF568) for 2 h to label endolysosomes, followed
807 by washes to remove unbound dextran. Cells were then imaged live by lattice light-sheet
808 microscopy during treatment with 50 nM apilimod in either glutamine-containing or glutamine-free
809 medium. Imaging was initiated simultaneously with apilimod addition.
810 **(B)** Representative maximum intensity z-projections from volumetric time series at t = 0, 9, 21,
811 and 30 min post-apilimod addition, with or without glutamine. Dextran-AF568–labeled
812 endolysosomes are shown in yellow. Scale bar, 10 μm and 1 μm in insets.
813 **(C)** Schematic of the infection assay. Vero cells were incubated with VSV-MeGFP–ZEBOV for 30
814 min, unbound virus was removed by three washes, and cells were treated for 30 min with 50 nM
815 apilimod or DMSO vehicle in either glutamine-containing or glutamine-free medium. Cells were
816 then transferred to glutamine-containing medium with 5 μM apilimod for the remainder of the
817 experiment. At 7.5 h postinfection, cells were fixed, and infection was quantified as the percentage
818 of MeGFP-positive cells relative to total number of cells identified by nuclear staining (Hoechst
819 Janelia 646). Automated analysis was performed using FIJI.
820 **(D)** Representative maximum intensity z-projections showing infected cells (MeGFP, green) and
821 nuclei stained with Hoechst Janelia 646 (magenta) under each condition.

822 **(E)** Quantification of infection. Data are shown as the percentage of infected cells normalized to
823 untreated control. Each biological replicate (n = 3) is shown in a different color; technical triplicates
824 are represented as same-colored dots. Approximately 16,000 cells were analyzed per condition.
825 Bars represent mean ± SD. Statistical significance was assessed by unpaired t test; *P < 0.05,
826 ****P < 0.0001.
827
828 **Figure 7. Hypotonic-induced endolysosome enlargement is dose-dependent and**
829 **correlates with inhibition of VSV-MeGFP–ZEBOV infection.**
830 **(A)** Schematic of the endolysosome enlargement assay. Vero cells not expressing TMPRSS2
831 were incubated with 10 μM Alexa Fluor 568–labeled dextran (Dextran-AF568) for 2 h to label
832 endolysosomes, followed by washes to remove unbound dextran. Cells were then exposed to
833 hypotonic media (0%, 10%, 30%, or 60%) for 10 min prior to imaging, which was performed using
834 live cell spinning disk confocal microscopy. Hypotonic conditions were maintained throughout
835 image acquisition.
836 **(B)** Representative maximum intensity z-projections showing Dextran-AF568 signal (yellow) in
837 cells exposed to increasing hypotonic medium. Enlarged endolysosomes are observed in 30%
838 and 60% conditions. Scale bar, 10 μm.
839 **(C)** Distribution of endolysosome radii for cells treated with 0% (black), 10% (blue), 30% (green),
840 or 60% (red) hypotonic media. Solid lines represent the mean endolysosome radius across all
841 cells per condition; shaded areas denote SD. Cell counts: N = 24 (0%), 32 (10%), 25 (30%), and
842 27 (60%). The gray shaded region marks the 90th percentile of endolysosome with a radius >
843 0.725 μm in control cells (0%).
844 **(D)** Percentage of endolysosomes with radius >0.725 μm, plotted against hypotonic media
845 concentration. Bars represent mean ± SD. Statistical significance was assessed by one-way
846 ANOVA compared to control; **P < 0.01, ****P < 0.0001. Comparisons with P > 0.05 are not
847 shown.
848 **(E)** Schematic of the infectivity assay. Vero cells were infected with VSV-MeGFP–ZEBOV (MOI
849 ~ 0.1) for 30 min. Unbound virus was removed by three washes, and cells were then treated with
850 0%, 10%, 30%, or 60% hypotonic media or 5 μM apilimod for 30 min. Following treatment, all
851 conditions were maintained in 5 μM apilimod for the duration of the experiment. At 7.5 h
852 postinfection, cells were fixed, and infection was quantified by establishing the ratio of cells
853 expressing MeGFP cytosolic fluorescence with respect to the total number of cells identified by
854 nuclear staining using automated image analysis in FIJI.

855 **(F)** Representative maximum intensity z-projections showing infected cells (MeGFP, green) and
856 nuclei stained with Hoechst Janelia 646 (magenta) for each treatment condition. Scale bar, 100
857 µm.
858 **(G)** Quantification of infection levels. Data are shown as the percentage of infected cells
859 normalized to the untreated control for each biological replicate (n = 3; distinct colors). Technical
860 triplicates appear as dots of the same color. Approximately 16,000 cells were analyzed per
861 condition. Bars represent mean ± SD. Statistical significance was assessed by one-way ANOVA;
862 ****P < 0.0001. Comparisons with P > 0.05 are not shown.
863
864 **Figure 8. Hypotonic stress partially inhibits infection by VSV-eGFP–SARS-CoV-2 and VSV-**
865 **MeGFP–ZEBOV, but not by VSV-eGFP–G.**
866 **(A)** Schematic of the infection assay. SVG-A or Vero cells not expressing TMPRRS2 were
867 incubated with VSV-eGFP–G, VSV-eGFP–SARS-CoV-2, or VSV-MeGFP–ZEBOV (MOI ~ 0.5)
868 for 30 min, followed by three washes to remove unbound virus. Cells were then treated with 0%
869 or 60% hypotonic medium for 30 min. Following treatment, cells were maintained in either 100
870 nM Bafilomycin A1 (used only for VSV-eGFP–G samples) or 5 µM apilimod (used for the other
871 virions) for the remainder of the experiment. At 7.5 h postinfection, cells were fixed, and infection
872 was quantified by counting GFP-positive cells relative to total nuclei (Hoechst Janelia 646) using
873 spinning disc confocal fluorescence microscopy. Automated analysis was performed in FIJI.
874 **(B-D)** Representative maximum intensity z-projection images (top) showing infected cells (eGFP,
875 green) and nuclei (magenta) under 0% and 60% hypotonic conditions for each type of virion.
876 Quantification of infection levels. Data (bottom) are shown as the percentage of infected cells
877 normalized to the untreated control for each biological replicate (n = 3; distinct colors). Technical
878 triplicates are represented as same-colored dots. Approximately 16,000 cells were analyzed per
879 condition. Bars represent mean ± SD. Statistical significance was assessed using an unpaired t
880 test; ****P < 0.0001. Comparisons with P > 0.05 are not shown.
881
882 **Figure 9. 3D tracking of VSV-MeGFP–ZEBOV reveals confined and membrane-bound virion**
883 **populations within apilimod-induced swollen NPC1-positive endolysosomes. Associated**
884 **with Movies 1-3.**
885 **(A)** Schematic of the infection assay. Gene-edited SVG-A cells expressing NPC1-Halo were
886 pretreated with 5 µM apilimod for 1 h, then incubated with VSV-MeGFP–ZEBOV (10 min, MOI ~
887 1) in the continued presence of apilimod. Unbound virus was removed by three washes (each
888 containing 5 µM apilimod), and cells were maintained in apilimod for the duration of the

889 experiment. Live-cell imaging was performed at 50 min postinfection using lattice light-sheet
890 microscopy. 3D time-lapse series were acquired every 4 s over 10 min.
891 **(B, C)** Representative 3D trajectories of individual virions moving within the lumen **(B)** or along
892 the limiting membrane **(C)** of NPC1-positive endolysosomes. NPC1-Halo–positive
893 endolysosomes are shown as gray spheres. Virion positions are color-coded over time (dark blue
894 to dark red). Associated maximum intensity z-projections show NPC1-Halo labeled with JF 646
895 (magenta) and VSV-MeGFP–ZEBOV (green). Mean square displacement (MSD) plots are
896 shown; in **(B)**, the radius of confinement is derived from the MSD plateau using the relationship
897 3/5 R^2 (inset).
898 **(D, E)** Simulated 3D trajectories recapitulating observed motion types. **(D)** A particle undergoing
899 confined motion within a spherical volume, with step length comparable to the radius. **(E)** Two
900 particles exhibiting membrane-bound movement on the surface of a rotating sphere at different
901 rotation speeds (blue and brown). MSD curves corresponding to the simulated trajectories are
902 shown.
903 **(F)** Quantification of the percentage of VSV-eGFP–G and VSV-MeGFP–ZEBOV virions exhibiting
904 membrane-bound trajectories compared to the total number of virions entrapped in NPC1-positive
905 endolysosomes. Analysis was based on movement patterns from 3D time-lapse maximum
906 intensity projections.
907
908 **Figure S1. Apilimod fails to induce swelling of early endosomes EEA1-positive/NPC1-**
909 **negative compartments (Related to Fig. 3).**
910 **(A)** Schematic of live cell imaging experiment. Gene-edited SVG-A cells expressing NPC1-Halo
911 labeled with JFX 646 and EEA1-mScarlet were pretreated with 5 μM apilimod for 1 h and imaged
912 live during a 10 min period, also in the presence of apilimod, using lattice light-sheet microscopy.
913 **(B, C)** Representative maximum intensity z-projections absence (control **(B)**) or presence **(C)** of
914 5 μM apilimod. NPC1-Halo labeled with JFX 646 is shown in magenta, and EEA1-mScarlet in
915 cyan. White arrowheads indicate early endosomes (EEA1-positive/NPC1-negative). Scale bar,
916 10 μm.
917 **(C)** Top panel presents EEA1 images with higher contrast to visualize dimmer early endosomes;
918 bottom panel presents the image in the same contrast as control **(B)**.
919
920 **Movies 1–3. Associated to Fig. 9 B and C.** Live-cell 3D time-lapse imaging of VSV-MeGFP–
921 ZEBOV virions (green) associated with endolysosomes enlarged by PIKfyve inhibition with
922 apilimod. SVG-A cells expressing gene-edited NPC1–Halo labeled with JF 646 (magenta). Cells

923 were pretreated with 5 μM apilimod for 1 h and then incubated with fluorescent VSV-MeGFP–
924 ZEBOV (10 min, MOI ~1) in the continued presence of apilimod. Live-cell imaging by LLSM was
925 performed 50 min postinfection. The 3D time-lapse series, acquired every 4 s for 10 min, are
926 displayed as maximum-intensity projections. Scale bar, 2 μm.

927 **REFERENCES**

928 1. Harrison, S. C. Viral membrane fusion. *Virology* **479**, 498–507 (2015).

929 2. Belouzard, S., Millet, J. K., Licitra, B. N. & Whittaker, G. R. Mechanisms of Coronavirus Cell
930 Entry Mediated by the Viral Spike Protein. *Viruses* **4**, 1011–1033 (2012).

931 3. Hofmann-Winkler, H., Kaup, F. & Pöhlmann, S. Host Cell Factors in Filovirus Entry: Novel
932 Players, New Insights. *Viruses* **4**, 3336–3362 (2012).

933 4. White, J. M. & Schornberg, K. L. A new player in the puzzle of filovirus entry. *Nat. Rev.*
934 *Microbiol.* **10**, 317–322 (2012).

935 5. Jackson, C. B., Farzan, M., Chen, B. & Choe, H. Mechanisms of SARS-CoV-2 entry into
936 cells. *Nat Rev Mol Cell Bio* **23**, 3–20 (2022).

937 6. Cai, X., Xu, Y., Kim, Y.-M., Loureiro, J. & Huang, Q. PIKfyve, a class III lipid kinase, is
938 required for TLR-induced type I IFN production via modulation of ATF3. *Journal of immunology*
939 *(Baltimore, Md : 1950)* **192**, 3383–3389 (2014).

940 7. Lartigue, J. de *et al.* PIKfyve Regulation of Endosome-Linked Pathways. *Traffic* **10**, 883–893
941 (2009).

942 8. Cerny, J. *et al.* The small chemical vacuolin-1 inhibits Ca(2+)-dependent lysosomal
943 exocytosis but not cell resealing. *EMBO reports* **5**, 883–888 (2004).

944 9. Sano, O. *et al.* Vacuolin-1 inhibits autophagy by impairing lysosomal maturation via PIKfyve
945 inhibition. *FEBS Lett.* **590**, 1576–1585 (2016).

946 10. Nelson, E. A. *et al.* The phosphatidylinositol-3-phosphate 5-kinase inhibitor apilimod blocks
947 filoviral entry and infection. *PLoS Neglected Trop. Dis.* **11**, e0005540 (2017).

948 11. Kang, Y.-L. *et al.* Inhibition of PIKfyve kinase prevents infection by Zaire ebolavirus and
949 SARS-CoV-2. *Proc National Acad Sci* **117**, 20803–20813 (2020).

950 12. Seo, Y. *et al.* A dual inhibitor of PIP5K1C and PIKfyve prevents SARS-CoV-2 entry into
951 cells. *Exp. Mol. Med.* **56**, 1736–1749 (2024).

952 13. Cuesta-Geijo, M. A. *et al.* Endosomal Maturation, Rab7 GTPase and Phosphoinositides in
953 African Swine Fever Virus Entry. *PLoS ONE* **7**, e48853 (2012).

954 14. Luo, Z. *et al.* Inhibition of PIKFYVE kinase interferes ESCRT pathway to suppress RNA
955 virus replication. *J. Méd. Virol.* **95**, e28527 (2023).

956 15. Drewry, D. H., Potjewyd, F. M., Smith, J. L., Howell, S. & Axtman, A. D. Identification of a
957 chemical probe for lipid kinase phosphatidylinositol-5-phosphate 4-kinase gamma (PI5P4Kγ).
958 *Curr. Res. Chem. Biol.* **3**, 100036 (2023).

959 16. Baker, J. *et al.* Pan-antiviral effects of a PIKfyve inhibitor on respiratory virus infection in
960 human nasal epithelium and mice. *Antimicrob. Agents Chemother.* **68**, e01050-23 (2023).

961 17. Yang, H. *et al.* LYVAC/PDZD8 is a lysosomal vacuolator. *Science* **389**, eadz0972 (2025).

962 18. Simmons, J. A. *et al.* Ebolavirus Glycoprotein Directs Fusion through NPC1+
963 Endolysosomes. *J. Virol.* **90**, 605–610 (2015).

964 19. Winter, S. L. *et al.* The Ebola virus VP40 matrix layer undergoes endosomal disassembly
965 essential for membrane fusion. *EMBO J.* **42**, EMBJ2023113578 (2023).

966 20. Koch, J. *et al.* TMPRSS2 expression dictates the entry route used by SARS-CoV-2 to infect
967 host cells. *Embo J* **40**, e107821 (2021).

968 21. Ou, T. *et al.* Hydroxychloroquine-mediated inhibition of SARS-CoV-2 entry is attenuated by
969 TMPRSS2. *Plos Pathog* **17**, e1009212 (2021).

970 22. Hoffmann, M. *et al.* SARS-CoV-2 Cell Entry Depends on ACE2 and TMPRSS2 and Is
971 Blocked by a Clinically Proven Protease Inhibitor. *Cell* **181**, 271-280.e8 (2020).

972 23. Kreutzberger, A. J. B. *et al.* Synergistic Block of SARS-CoV-2 Infection by Combined Drug
973 Inhibition of the Host Entry Factors PIKfyve Kinase and TMPRSS2 Protease. *J. Virol.* **95**,
974 10.1128/jvi.00975-21 (2021).

975 24. Uwada, J. *et al.* PIKFYVE inhibition induces endosome- and lysosome-derived vacuole
976 enlargement via ammonium accumulation. *J. Cell Sci.* **138**, (2025).

977 25. Compton, L. M., Ikonomov, O. C., Sbrissa, D., Garg, P. & Shisheva, A. Active vacuolar H+
978 ATPase and functional cycle of Rab5 are required for the vacuolation defect triggered by
979 PtdIns(3,5)P2 loss under PIKfyve or Vps34 deficiency. *American journal of physiology Cell*
980 *physiology* **311**, C366-77 (2016).

981 26. Zook, E. *et al.* Delayed vacuolation in mammalian cells caused by hypotonicity and ion loss.
982 *Sci. Rep.* **14**, 29354 (2024).

983 27. King, C., Sengupta, P., Seo, A. Y. & Lippincott-Schwartz, J. ER membranes exhibit phase
984 behavior at sites of organelle contact. *Proc. Natl. Acad. Sci.* **117**, 7225–7235 (2020).

985 28. Li, P. *et al.* LRRC8 family proteins within lysosomes regulate cellular osmoregulation and
986 enhance cell survival to multiple physiological stresses. *Proc. Natl. Acad. Sci.* **117**, 29155–
987 29165 (2020).

988 29. Bowman, E. J., Siebers, A. & Altendorf, K. Bafilomycins: a class of inhibitors of membrane
989 ATPases from microorganisms, animal cells, and plant cells. *Proc. Natl. Acad. Sci.* **85**, 7972–
990 7976 (1988).

991 30. Leray, X. *et al.* Tonic inhibition of the chloride/proton antiporter ClC-7 by PI(3,5)P2 is crucial
992 for lysosomal pH maintenance. *eLife* **11**, e74136 (2022).

993 31. Sharma, G. *et al.* A family of PIKFYVE inhibitors with therapeutic potential against
994 autophagy-dependent cancer cells disrupt multiple events in lysosome homeostasis. *Autophagy*
995 **15**, 1694–1718 (2019).

996 32. Johannsdottir, H. K., Mancini, R., Kartenbeck, J., Amato, L. & Helenius, A. Host cell factors
997 and functions involved in vesicular stomatitis virus entry. *J Virol* **83**, 440–453 (2009).

998 33. Mire, C. E., White, J. M. & Whitt, M. A. A Spatio-Temporal Analysis of Matrix Protein and
999 Nucleocapsid Trafficking during Vesicular Stomatitis Virus Uncoating. *PLoS Pathog.* **6**,
1000 e1000994 (2010).

1001 34. Sieczkarski, S. B. & Whittaker, G. R. Differential Requirements of Rab5 and Rab7 for
1002 Endocytosis of Influenza and Other Enveloped Viruses. *Traffic* **4**, 333–343 (2003).

1003 35. White, J. M. & Whittaker, G. R. Fusion of Enveloped Viruses in Endosomes. *Traffic* **17**, 593–
1004 614 (2016).

1005 36. Zang, R. *et al.* TMPRSS2 and TMPRSS4 promote SARS-CoV-2 infection of human small
1006 intestinal enterocytes. *Sci. Immunol.* **5**, eabc3582 (2020).

1007 37. Whelan, S. P., Ball, L. A., Barr, J. N. & Wertz, G. T. Efficient recovery of infectious vesicular
1008 stomatitis virus entirely from cDNA clones. *Proc. Natl. Acad. Sci.* **92**, 8388–8392 (1995).

1009 38. Si, Z., Zhou, K., Tsao, J., Luo, M. & Zhou, Z. H. Locations and in situ structure of the
1010 polymerase complex inside the virion of vesicular stomatitis virus. *Proc. Natl. Acad. Sci.* **119**,
1011 e2111948119 (2022).

1012 39. Case, J. B. *et al.* Neutralizing Antibody and Soluble ACE2 Inhibition of a Replication-
1013 Competent VSV-SARS-CoV-2 and a Clinical Isolate of SARS-CoV-2. *Cell host & microbe* **28**,
1014 475-485.e5 (2020).

1015 40. Wong, A. C., Sandesara, R. G., Mulherkar, N., Whelan, S. P. & Chandran, K. A forward
1016 genetic strategy reveals destabilizing mutations in the Ebolavirus glycoprotein that alter its
1017 protease dependence during cell entry. *Journal of virology* **84**, 163–175 (2010).

1018 41. Zhou, K. *et al.* Atomic model of vesicular stomatitis virus and mechanism of assembly. *Nat.*
1019 *Commun.* **13**, 5980 (2022).

1020 42. Arzt, M. *et al.* LABKIT: Labeling and Segmentation Toolkit for Big Image Data. *Front.*
1021 *Comput. Sci.* **4**, (2022).

1022 43. Aguet, F. *et al.* Membrane dynamics of dividing cells imaged by lattice light-sheet
1023 microscopy. *Molecular biology of the cell* (2016) doi:10.1091/mbc.e16-03-0164.

1024 44. Thomas, L. S. V. & Gehrig, J. Multi-template matching: a versatile tool for object-localization
1025 in microscopy images. *BMC Bioinform.* **21**, 44 (2020).

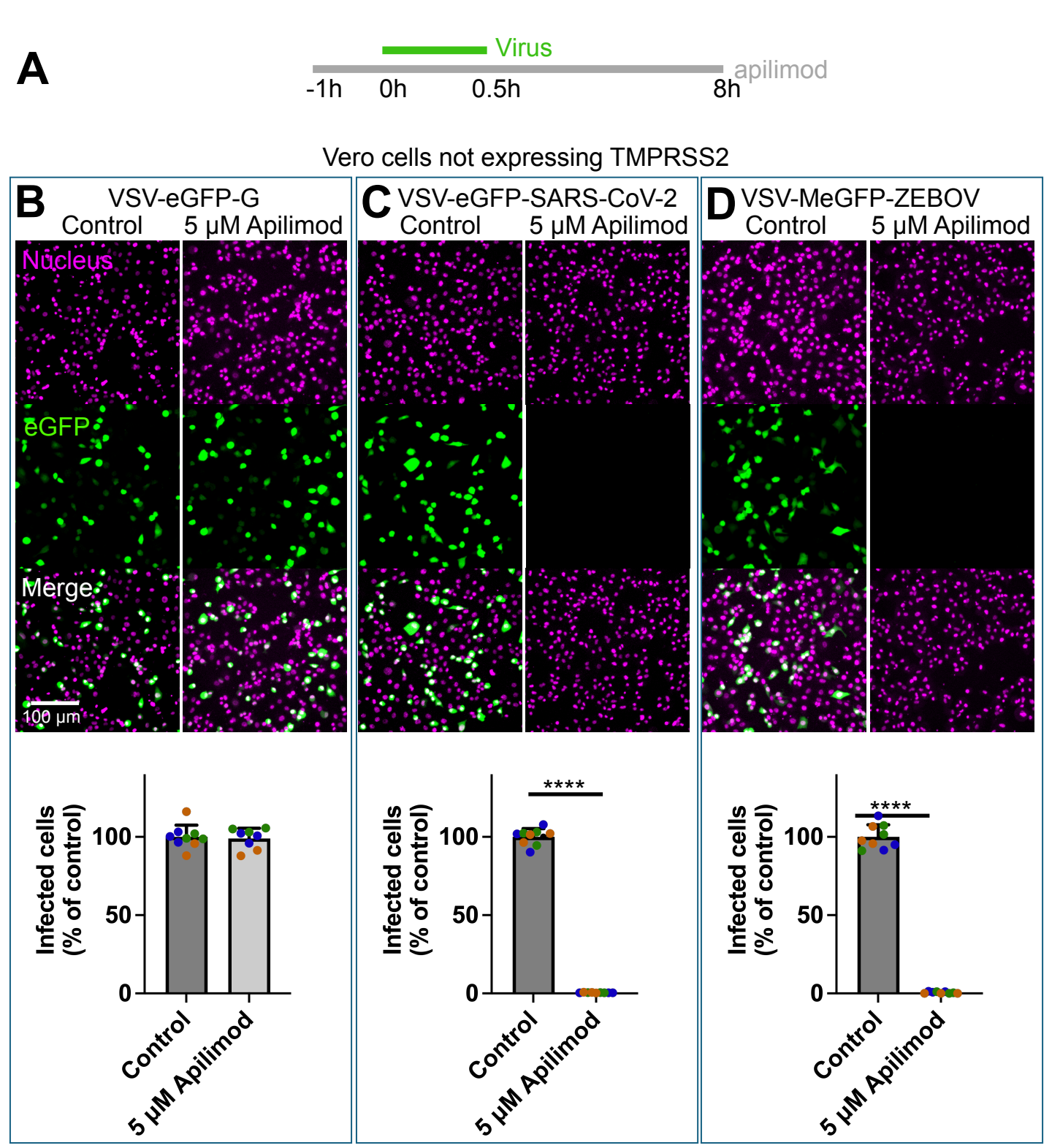
A
Virus
apilimod
-1h
0h
0.5h
8h
Vero cells not expressing TMPRSS2
B
VSV-eGFP-G
Control
5 µM Apilimod
Nucleus
eGFP
Merge
100 µm
Infected cells (% of control)
100
50
0
Control
5 µM Apilimod
C
VSV-eGFP-SARS-CoV-2
Control
5 µM Apilimod
****
Infected cells (% of control)
100
50
0
Control
5 µM Apilimod
D
VSV-MeGFP-ZEBOV
Control
5 µM Apilimod
****
Infected cells (% of control)
100
50
0
Control
5 µM Apilimod

Figure 1

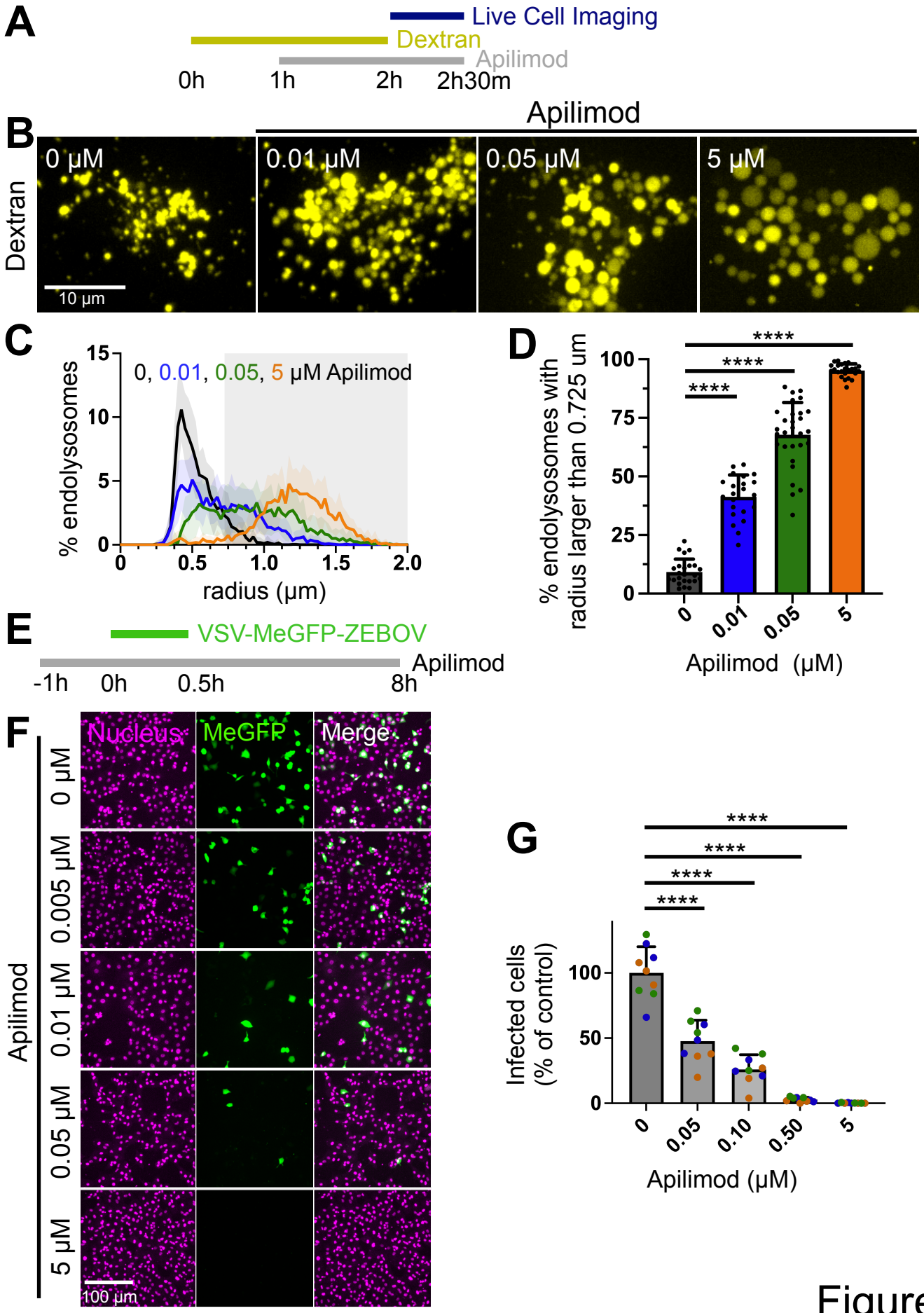
A
Live Cell Imaging
Dextran
Apilimod
0h
1h
2h
2h30m
B
Apilimod
Dextran
0 μM
0.01 μM
0.05 μM
5 μM
10 μm
C
0, 0.01, 0.05, 5 μM Apilimod
% endolysosomes
radius (μm)
D
% endolysosomes with radius larger than 0.725 um
Apilimod (μM)
E
VSV-MeGFP-ZEBOV
Apilimod
-1h
0h
0.5h
8h
F
Nucleus
MeGFP
Merge
Apilimod
0 μM
0.005 μM
0.01 μM
0.05 μM
5 μM
100 μm
G
Infected cells (% of control)
Apilimod (μM)

Figure 2

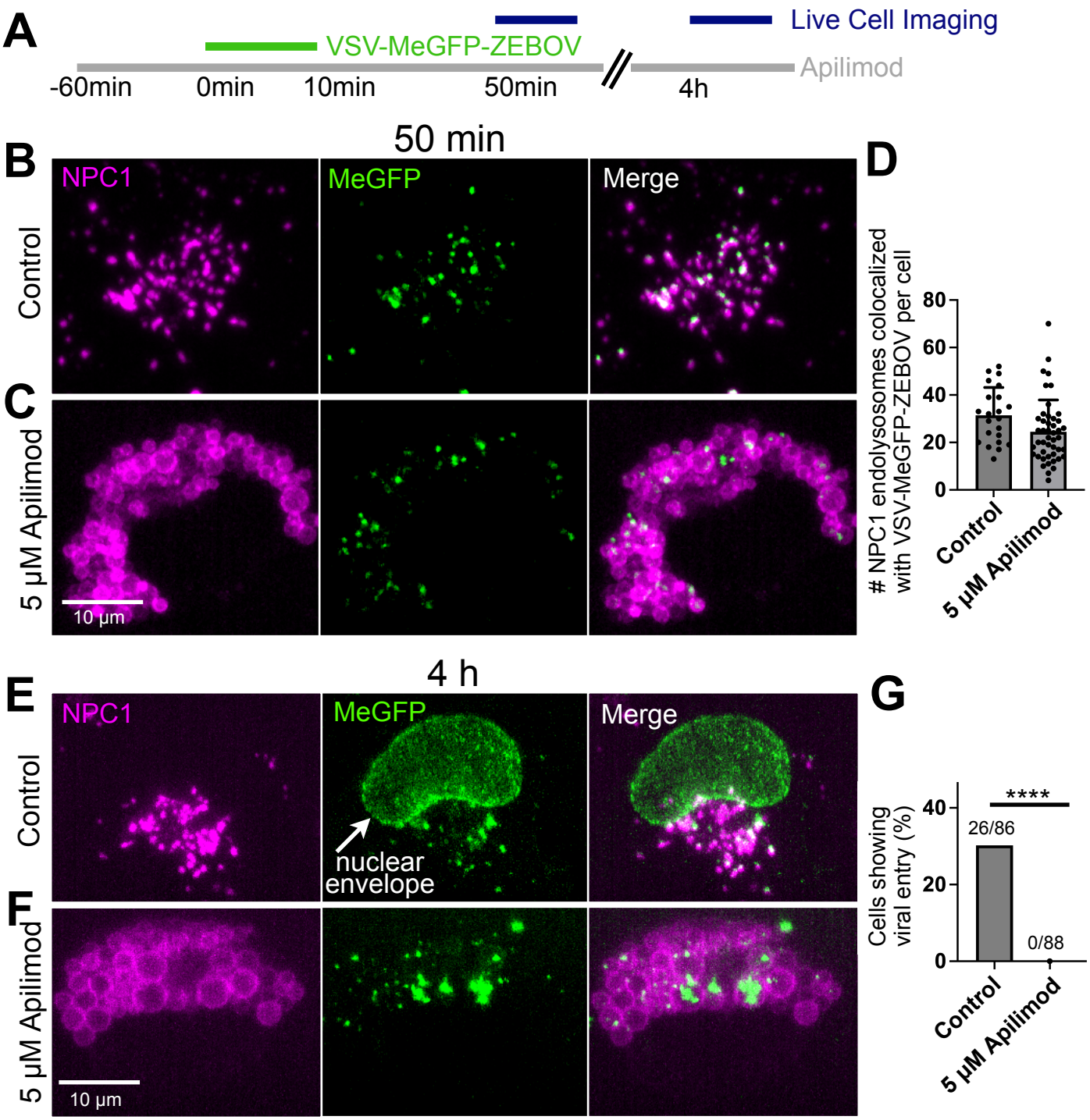
A
Live Cell Imaging
VSV-MeGFP-ZEBOV
Apilimod
-60min
0min
10min
50min
4h
50 min
B
NPC1
MeGFP
Merge
Control
C
5 µM Apilimod
10 µm
D
NPC1 endolysosomes colocalized with VSV-MeGFP-ZEBOV per cell
80
60
40
20
0
Control
5 µM Apilimod
4 h
E
NPC1
MeGFP
Merge
Control
nuclear envelope
F
5 µM Apilimod
10 µm
G
Cells showing viral entry (%)
40
20
0
****
26/86
0/88
Control
5 µM Apilimod

Figure 3

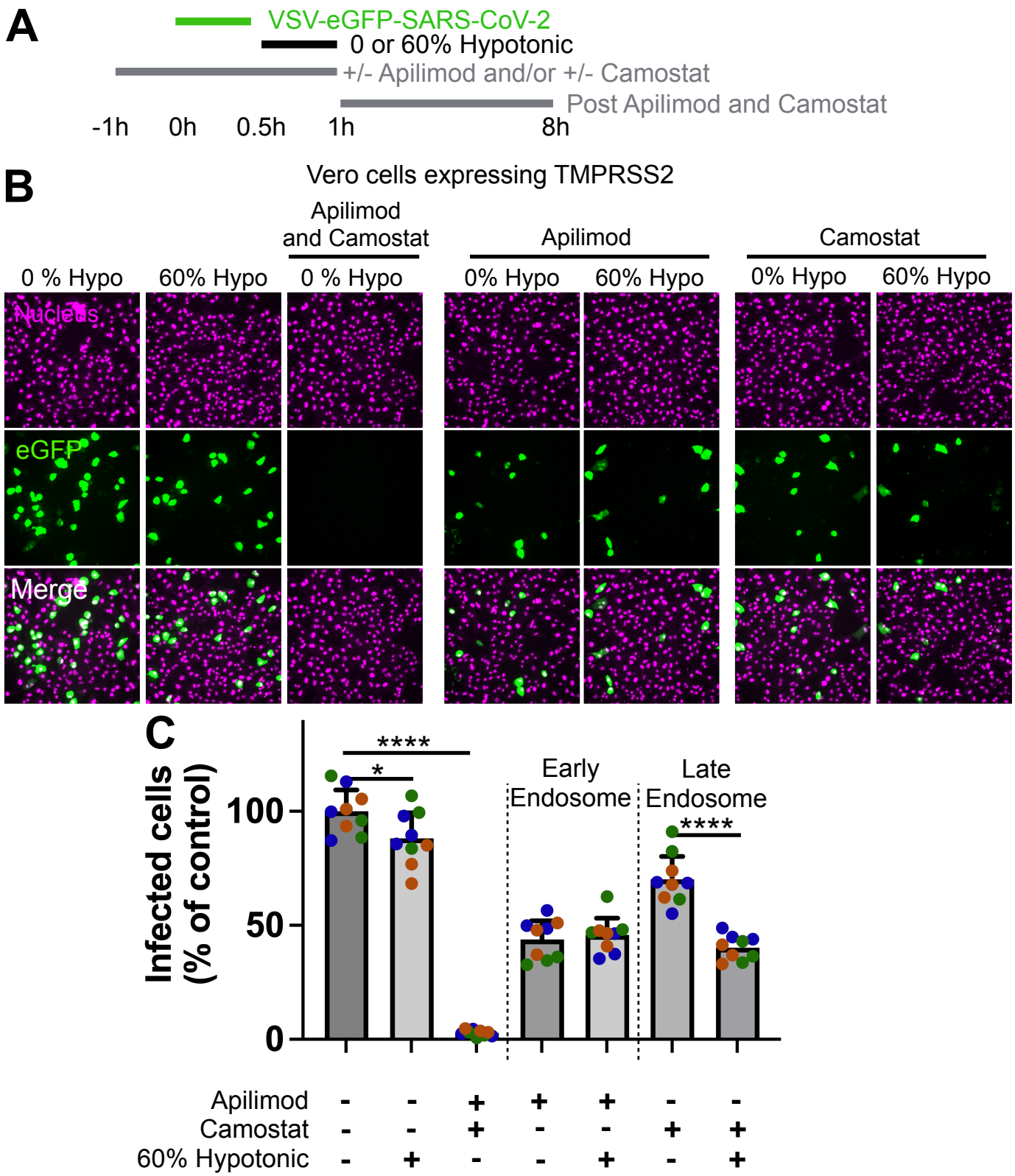
A
VSV-eGFP-SARS-CoV-2
0 or 60% Hypotonic
+/- Apilimod and/or +/- Camostat
Post Apilimod and Camostat
-1h
0h
0.5h
1h
8h
B
Vero cells expressing TMPRSS2
Apilimod and Camostat
Apilimod
Camostat
0 % Hypo
60% Hypo
0 % Hypo
0% Hypo
60% Hypo
0% Hypo
60% Hypo
Nucleus
eGFP
Merge
C
Infected cells (% of control)
100
50
0
****
*
Early Endosome
Late Endosome
****
Apilimod - - + + + - -
Camostat - - + - - + +
60% Hypotonic - + - - + - +

Figure 4

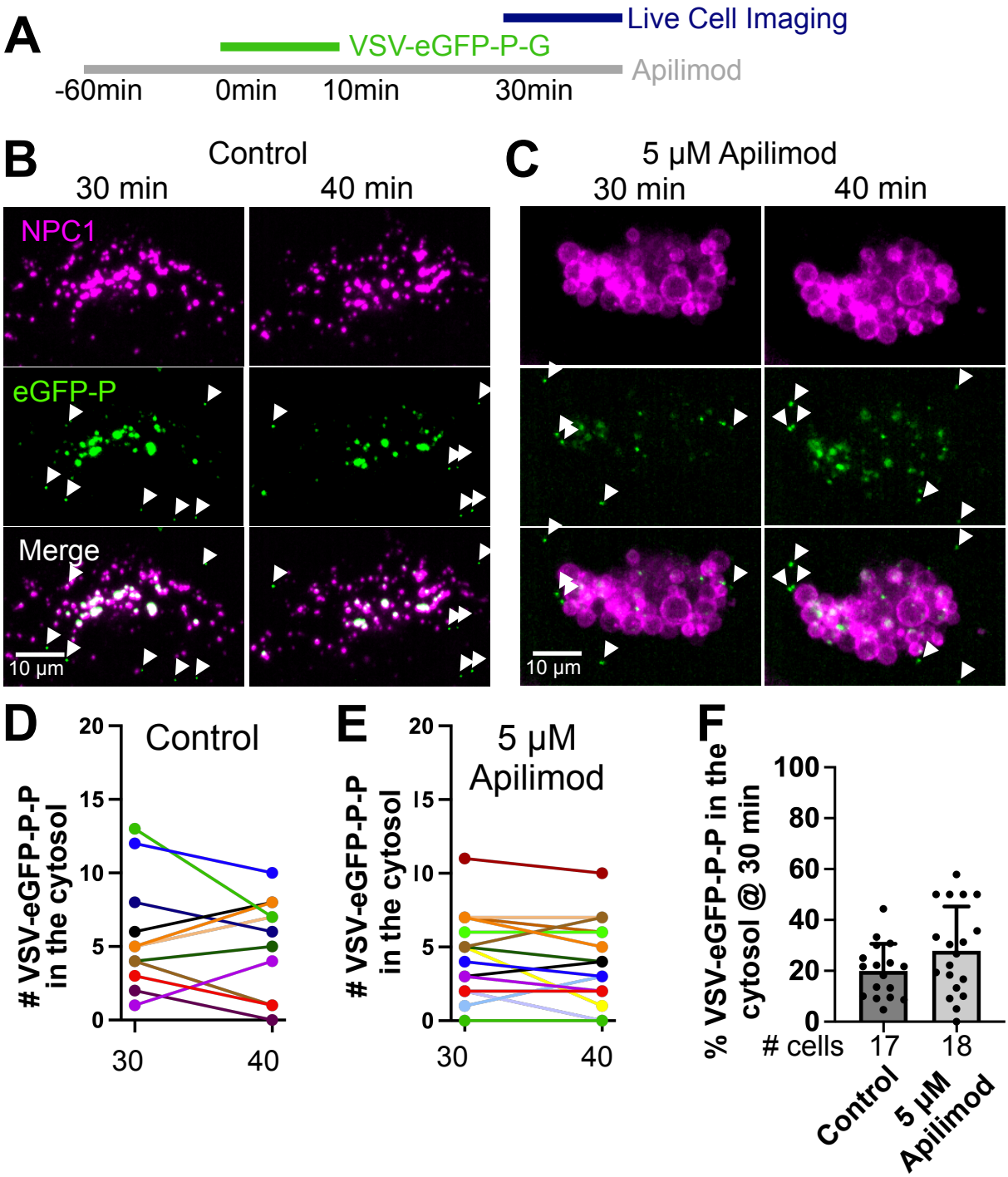
A
Live Cell Imaging
VSV-eGFP-P-G
Apilimod
-60min
0min
10min
30min
B
Control
30 min
40 min
NPC1
eGFP-P
Merge
10 µm
C
5 µM Apilimod
30 min
40 min
10 µm
D
Control
VSV-eGFP-P-P in the cytosol
20
15
10
5
0
30
40
E
5 µM Apilimod
VSV-eGFP-P-P in the cytosol
20
15
10
5
0
30
40
F
% VSV-eGFP-P-P in the cytosol @ 30 min
100
80
60
40
20
0
cells
17
18
Control
5 µM Apilimod

Figure 5

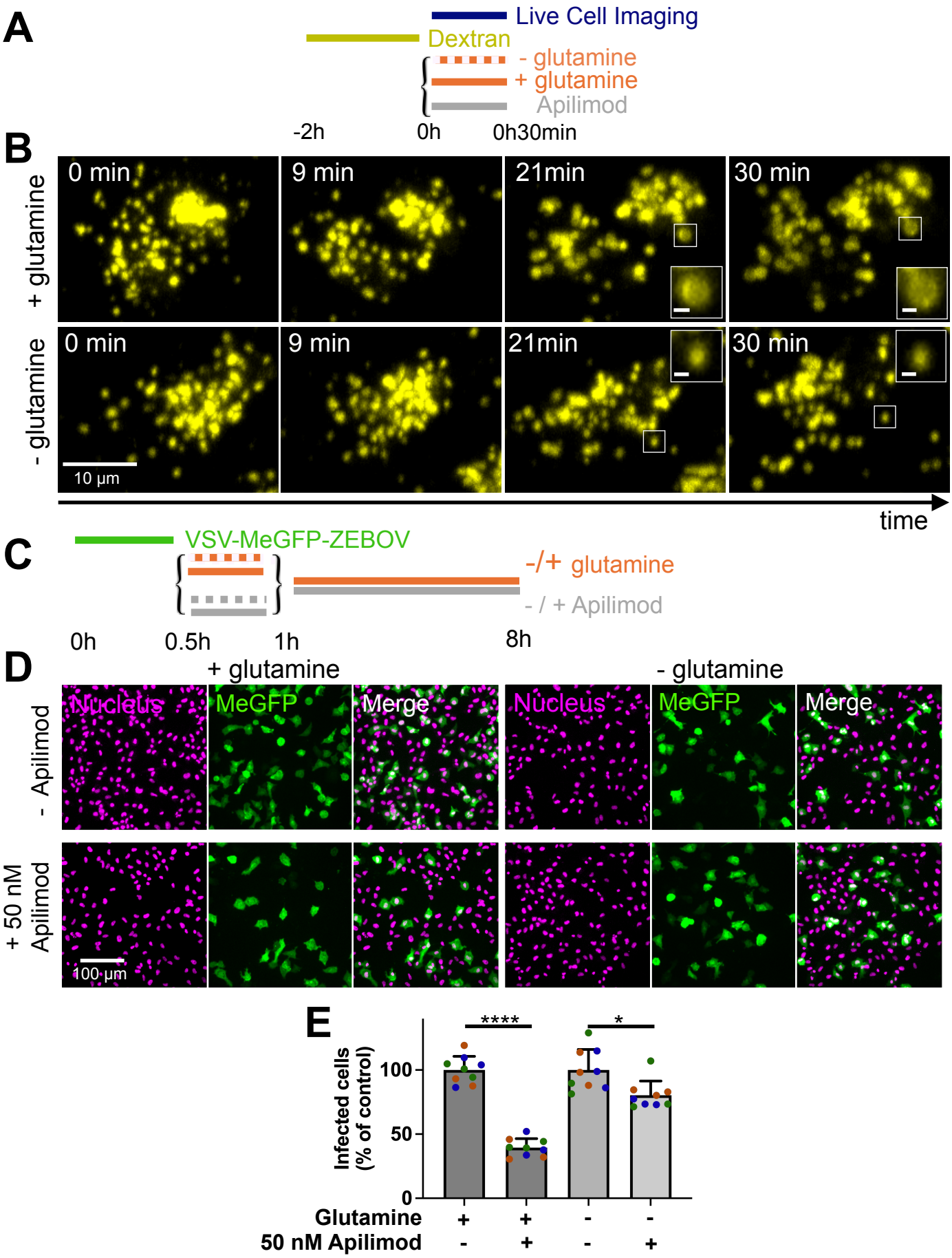
A
Live Cell Imaging
Dextran
- glutamine
+ glutamine
Apilimod
-2h
0h
0h30min
B
+ glutamine
- glutamine
0 min
9 min
21min
30 min
10 µm
time
C
VSV-MeGFP-ZEBOV
-/+ glutamine
- / + Apilimod
0h
0.5h
1h
8h
D
+ glutamine
- glutamine
- Apilimod
+ 50 nM Apilimod
Nucleus
MeGFP
Merge
100 µm
E
Infected cells (% of control)
100
50
0
****
*
Glutamine
50 nM Apilimod

Figure 6

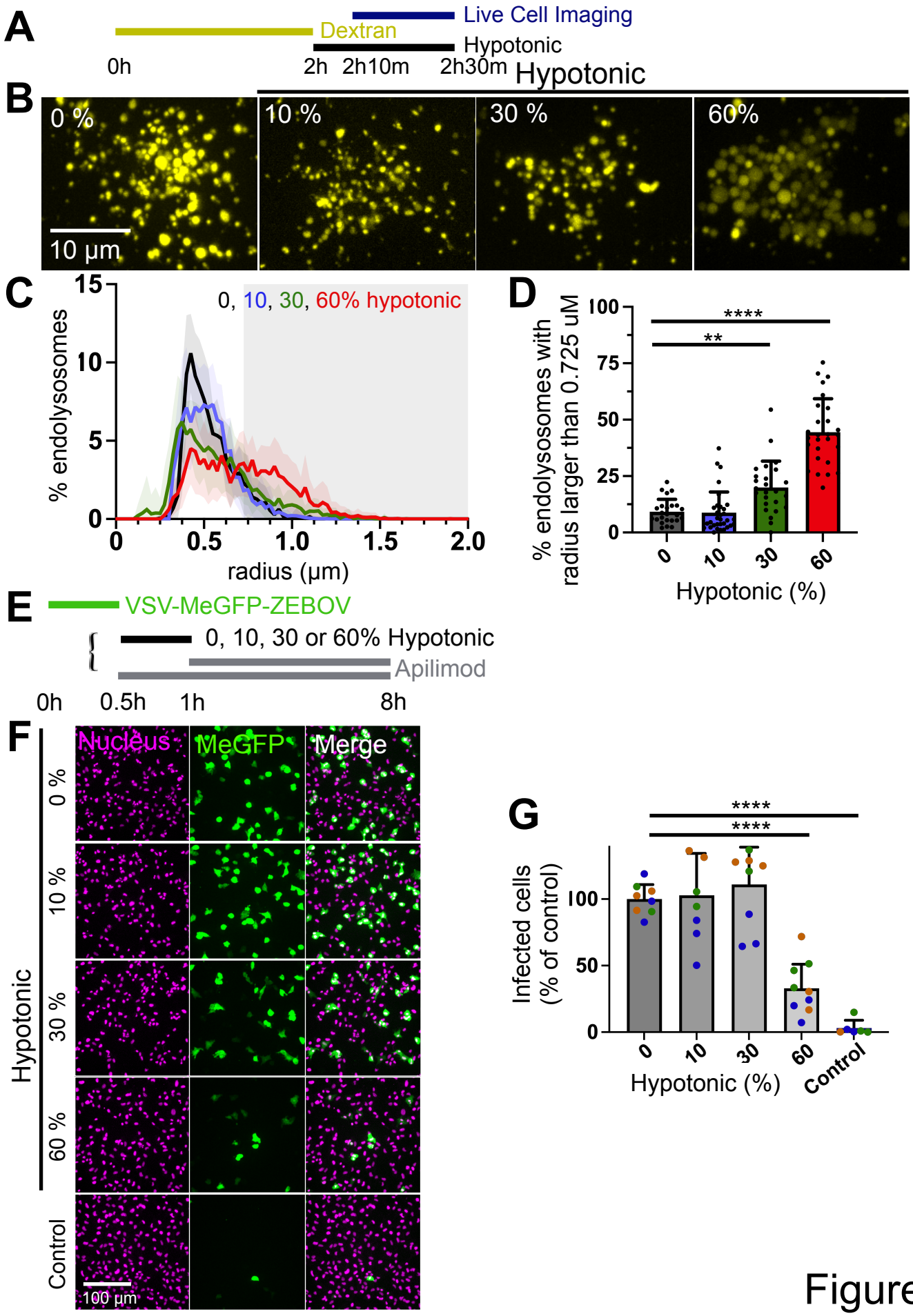
A
Live Cell Imaging
Dextran
Hypotonic
0h
2h
2h10m
2h30m
B
Hypotonic
0 %
10 %
30 %
60%
10 µm
C
0, 10, 30, 60% hypotonic
% endolysosomes
radius (µm)
D
% endolysosomes with radius larger than 0.725 uM
Hypotonic (%)
E
VSV-MeGFP-ZEBOV
0, 10, 30 or 60% Hypotonic
Apilimod
0h
0.5h
1h
8h
F
Nucleus
MeGFP
Merge
Hypotonic
0 %
10 %
30 %
60 %
Control
100 µm
G
Infected cells (% of control)
Hypotonic (%)
Control

Figure 7

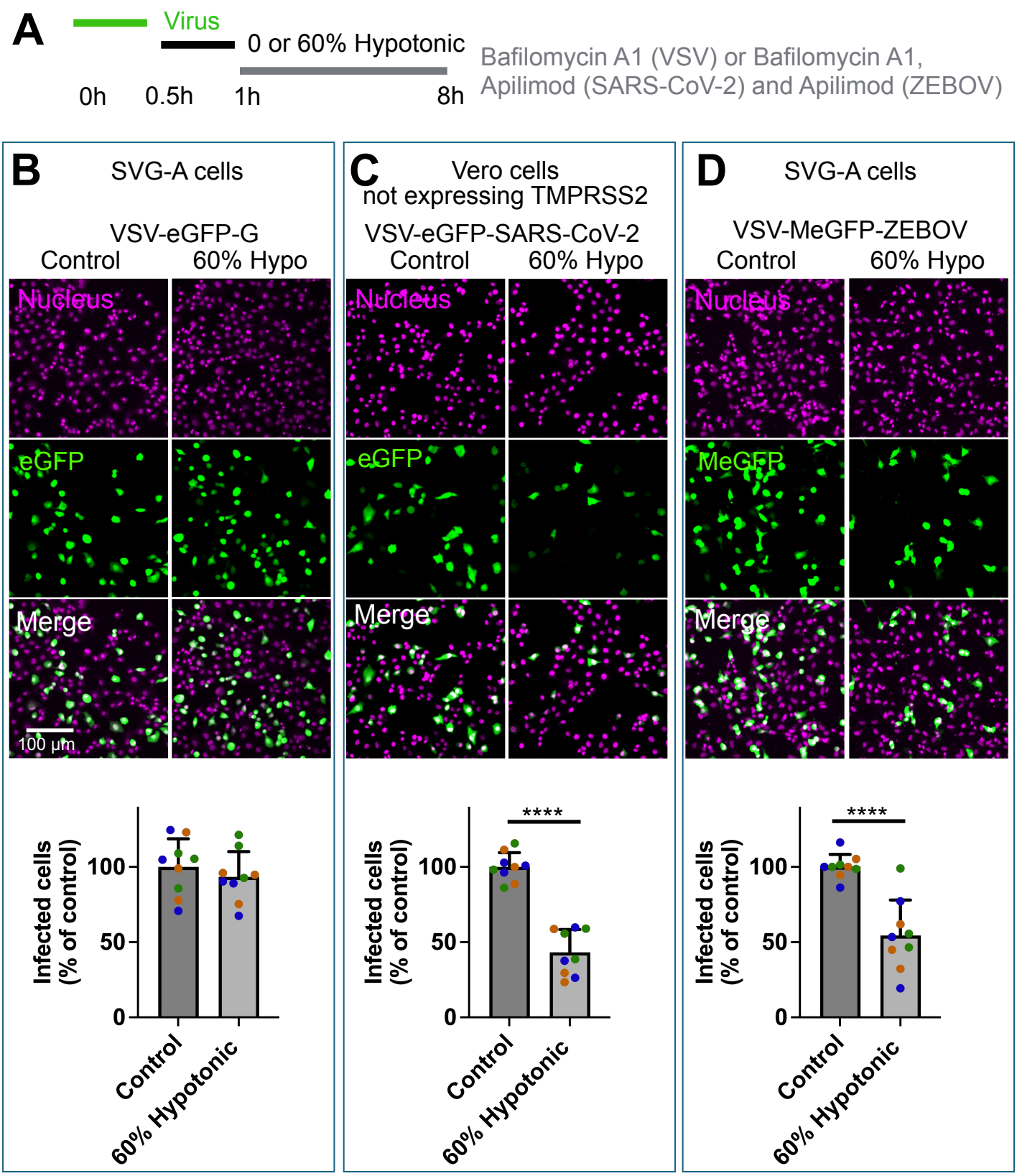
A
Virus
0 or 60% Hypotonic
Bafilomycin A1 (VSV) or Bafilomycin A1, Apilimod (SARS-CoV-2) and Apilimod (ZEBOV)
0h
0.5h
1h
8h
B
SVG-A cells
VSV-eGFP-G
Control
60% Hypo
Nucleus
eGFP
Merge
100 µm
Infected cells (% of control)
100
50
0
Control
60% Hypotonic
C
Vero cells not expressing TMPRSS2
VSV-eGFP-SARS-CoV-2
Control
60% Hypo
Nucleus
eGFP
Merge
****
Infected cells (% of control)
100
50
0
Control
60% Hypotonic
D
SVG-A cells
VSV-MeGFP-ZEBOV
Control
60% Hypo
Nucleus
MeGFP
Merge
****
Infected cells (% of control)
100
50
0
Control
60% Hypotonic

Figure 8

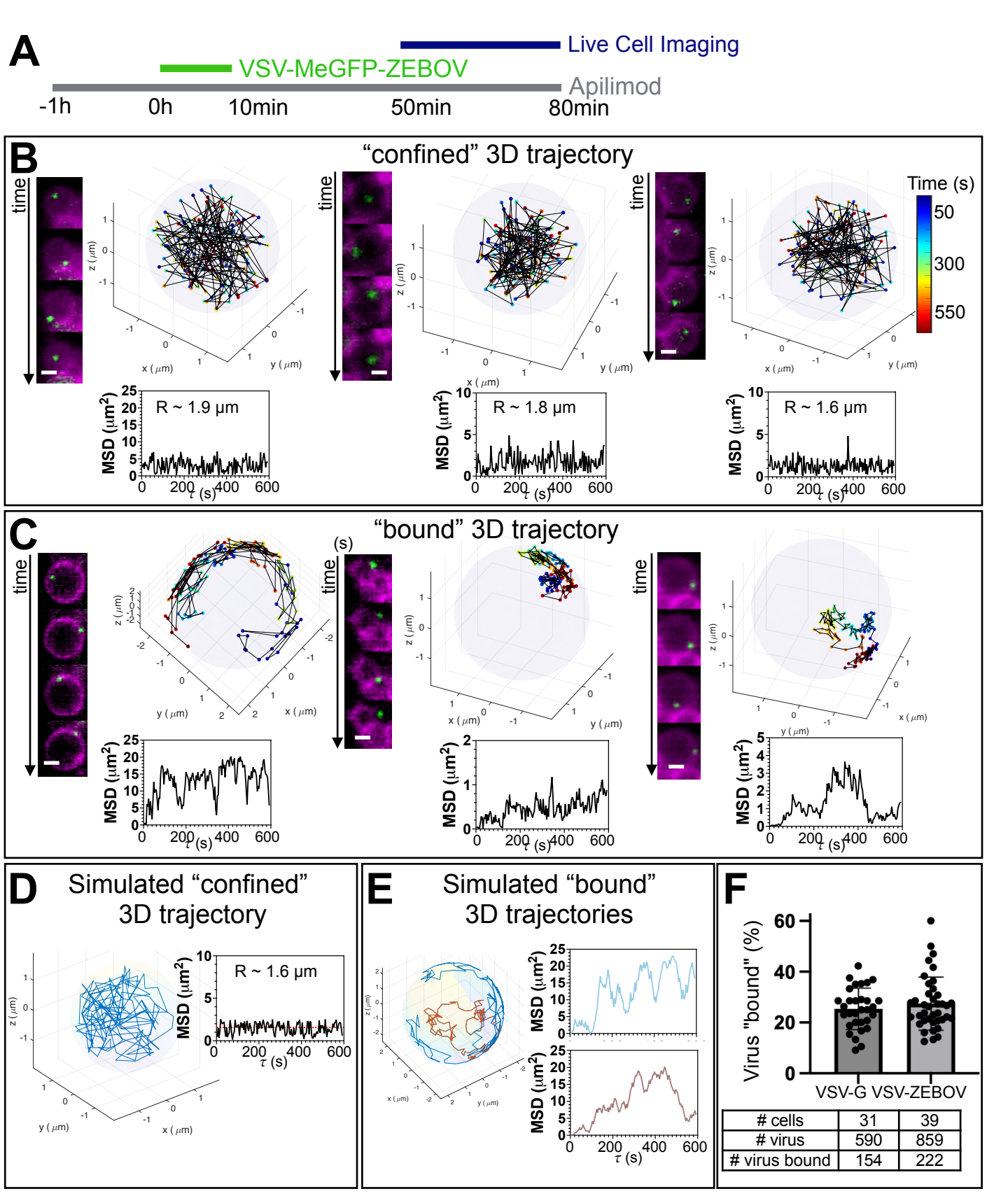
A
Live Cell Imaging
VSV-MeGFP-ZEBOV
Apilimod
-1h
0h
10min
50min
80min
B
"confined" 3D trajectory
time
Time (s)
50
300
550
R ~ 1.9 µm
R ~ 1.8 µm
R ~ 1.6 µm
MSD (µm²)
τ (s)
x (µm)
y (µm)
z (µm)
C
"bound" 3D trajectory
(s)
D
Simulated "confined" 3D trajectory
R ~ 1.6 µm
E
Simulated "bound" 3D trajectories
F
Virus "bound" (%)
VSV-G
VSV-ZEBOV
cells 31 39
virus 590 859
virus bound 154 222

Figure 9

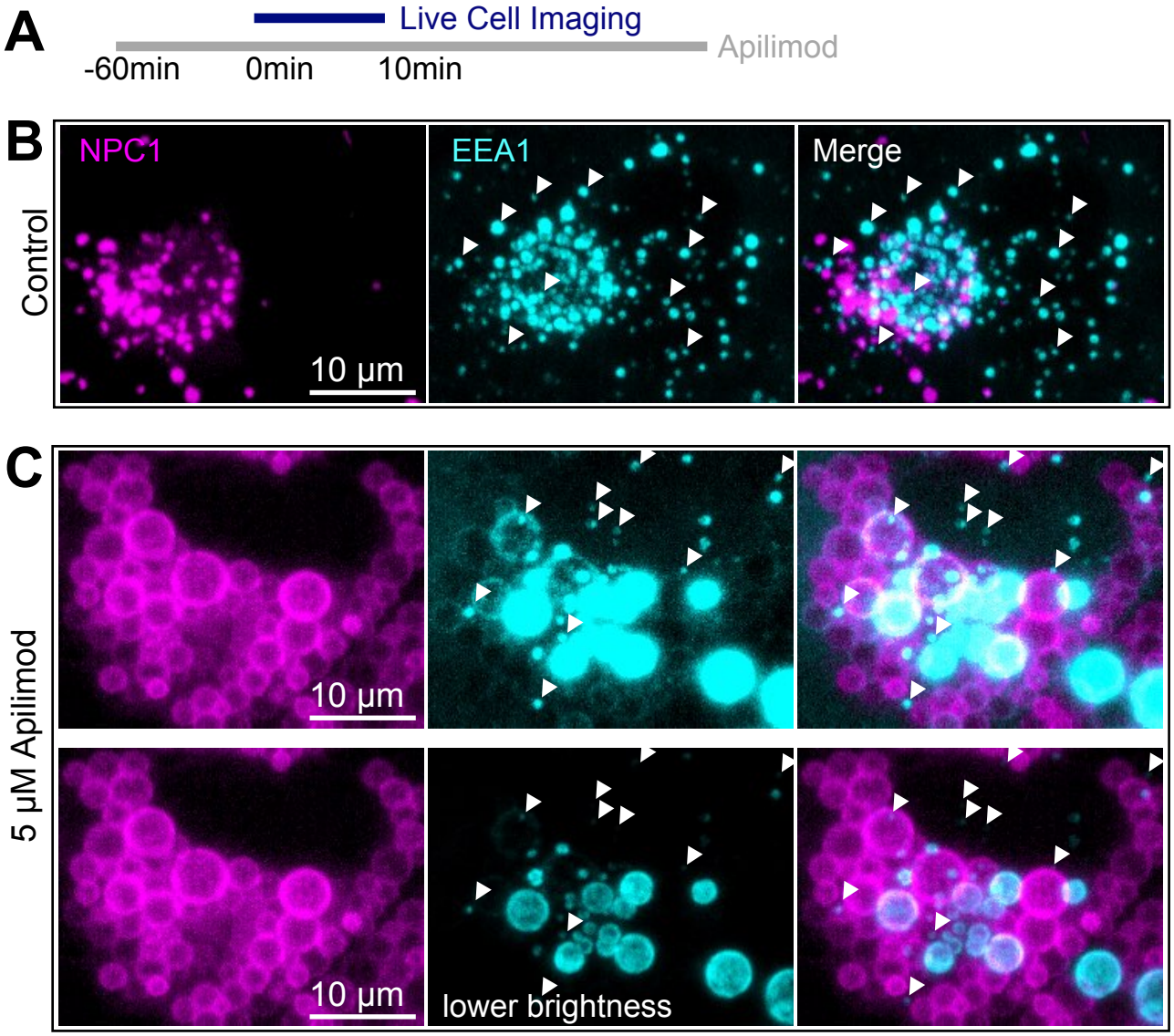
A
Live Cell Imaging
Apilimod
-60min
0min
10min
B
Control
NPC1
EEA1
Merge
10 µm
C
5 µM Apilimod
10 µm
10 µm
lower brightness

Fig S1